ADVANCED ENERGY & SUSTAINABILITY RESEARCH
Open Access
www.advenergysustres.com

Molybdenum-Based Catalytic Materials for Li–S Batteries: Strategies, Mechanisms, and Prospects

Yuping Liu, Zhihua Lin, Frederik Bettels, Zhenhu Li, Jingjing Xu, Yulin Zhang, Xu Li, Fei Ding, Shuangyi Liu,* and Lin Zhang**

Lithium–sulfur (Li–S) batteries are regarded as promising candidates for high-energy storage devices because of their high theoretical energy density (2600 Wh kg^{-1}). However, their practical applications are still hindered by a multitude of key challenges, especially the shuttle effect of soluble lithium polysulfides (LiPSs) and the sluggish sulfur redox kinetics. To address these challenges, varieties of catalytic materials have been exploited to prevent the shuttle effect and accelerate the LiPSs conversion. Recently, molybdenum-based (Mo-based) catalytic materials are widely used as sulfur host materials, modified separators, and interlayers for Li–S batteries. They include the Mo sulfides, diselenides, carbides, nitrides, oxides, phosphides, borides, and metal/single atoms/clusters. Here, recent advances in these Mo-based catalytic materials are comprehensively summarized, and the current challenges and prospects for designing highly efficient Mo-based catalytic materials are highlighted, with the aim to provide a fundamental understanding of the sulfur reaction mechanism, and to guide the rational design of cathode catalysts for high-energy and long-life Li–S batteries.

1. Introduction

The international market for energy storage systems (ESSs) has experienced rapid growth over the past few decades, however, the state-of-the-art EESs cannot keep up with the demand for grid-connected storage systems.[1] Thus, batteries with higher energy/power densities and lower production costs are urgently needed. Among various battery candidates, Li–S battery is considered one of the most attractive choices, because of their high theoretical energy density (2600 Wh kg^{-1}, more than five times of the traditional lithium-ion (Li-ion) batteries). Furthermore, the sulfur cathode has the advantages of natural abundance, environmental friendliness, and low cost.[2] Nevertheless, there are still several challenges to be resolved, including, 1) the intrinsic poor electrical conductivities of sulfur and Li_2S (5×10^{-30} S cm^{-1} and 10^{-30} S cm^{-1}, respectively) hinder the electron transfer and slow down the reaction kinetics; 2) the large volumetric changes during the lithiation/delithiation of S/Li_2S; 3) the shuttle effect of the soluble lithium polysulfide intermediates (LiPSs) leads to self-discharging and fast capacity decay; 4) the unstable solid electrolyte interfase (SEI) of Li anode during the cycling.[2b,3]

Tremendous efforts have been devoted to addressing these challenges over the past few decades. Many works focused on developing the conductive framework and the sulfur adsorbent. A variety of carbon-based hosts with porous structures have been widely investigated to facilitate the electron transfer and physical confinement of the soluble LiPSs. However, these strategies demonstrated only limited effects on suppressing the shuttle effect, due to the weak van der Waals interactions between the nonpolar carbon and the polar LiPSs.[3a,4] In this regard, the modification of carbon-based host by using heteroatoms (e.g., N, O, *P*-doping) and polar adsorbents (e.g., metal oxides and metal sulfides) were proposed. Although these approaches can efficiently suppress the shuttle effect, they do not yet meet the stringent demand for commercial applications.[5]

Moreover, for a number of applications, the batteries need to achieve not only high energy density but also high-power density. This is especially the case in contemporary electric vehicles (e.g., during acceleration and uphill driving) and in grid/home energy storage. Therefore, high sulfur mass loadings, low electrolyte/sulfur (E/S) ratio, and large current density are also required for Li–S batteries.[6] However, these working parameters exacerbate the intrinsic Li–S problems, for instance, the sluggish redox kinetics and shuttle effect will result in low sulfur

Y. Liu, Z. Li, J. Xu, Y. Zhang, X. Li, S. Liu
Research Center for Electrochemical Energy Storage Technologies
Chongqing Institute of Green and Intelligent Technology
Chinese Academy of Sciences
Chongqing 400714, P. R. China
E-mail: liuyuping@cigit.ac.cn; liushuangyi@cigit.ac.cn

Y. Liu, Z. Lin, F. Bettels, F. Ding, L. Zhang
Institute of Solid State Physics
Leibniz University Hannover
30167 Hannover, Germany
E-mail: lin.zhang@fkp.uni-hannover.de

Y. Liu, Z. Lin, F. Bettels, F. Ding, L. Zhang
Laboratory of Nano and Quantum Engineering (LNQE)
Leibniz University Hannover
Hannover 30167, Germany

The ORCID identification number(s) for the author(s) of this article can be found under https://doi.org/10.1002/aesr.202200145.

DOI: 10.1002/aesr.202200145

utilization and poor Columbic efficiency (CE), especially during the oxidation/reduction processes between the liquid (LiPSs)/solid (Li_2S_2/Li_2S) phases. The high activation barrier of the Li_2S reduction process accelerates the deposition of Li_2S on the Li metal surface and hence causes the dramatical capacity decay within a limited cycling number.[7]

In light of this, many research strategies shift from blocking the dissolution of LiPSs to accelerating the redox kinetics between the LiPSs and Li_2S_2/Li_2S. These "electrocatalyst" materials can decrease the activation energy of redox LiPSs and accelerate the ions/electron transport.[8] The shuttle effect is therefore greatly suppressed and the electrochemical performances are significantly improved. This strategy has been applied to a number of Li–S systems, including metal oxides,[9] metal sulfides,[10] metal nitrides,[11] metal carbides,[12] heterostructures,[13] and single atoms.[14] Interestingly, many of these electrocatalysts are molybdenum-based (Mo-based), including Mo sulfides, diselenides, carbides, nitrides, oxides, phosphides, borides, and metal/single atoms/clusters. Although there have been excellent overall reviews on the electrocatalysts in Li–S batteries,[3e,15] a dedicated summary on the highly efficient Mo-based catalysts in Li–S batteries does not yet exist. Therefore, this review aims to present a comprehensive and insightful overview of Mo-based catalysts. The current challenges and prospects in this field are highlighted, providing a fundamental understanding of the sulfur reaction mechanism and guiding the rational design of cathode catalysts for high-energy and long-life Li–S batteries.

2. Catalytic Materials for the Conversion of LiPSs

The utilization of sulfur as electrode material was first presented by Herbet and Ulam in 1962.[16] During the discharge, octasulfur proceeds through multiple steps[17]

$$S_8 + 2e^- \rightarrow S_8^{2-} \quad (1)$$

$$3S_8^{2-} + 2e^- \rightarrow 4S_6^{2-} \quad (2)$$

$$2S_6^{2-} + 2e^- \rightarrow 3S_4^{2-} \quad (3)$$

$$S_4^{2-} + 4Li^+ + 2e^- \rightarrow 2Li_2S_2 \quad (4)$$

$$Li_2S_2 + 2Li^+ + 2e^- \rightarrow 2Li_2S \quad (5)$$

The first three steps correspond to the transformation from solid S_8 to the liquid high-order lithium polysulfides (LiPSs) (Li_2S_x, $4 \leq x \leq 8$) in the voltage profile (2.3 V), and the LiPSs species produced in these steps are soluble in the electrolyte (**Figure 1**a). Although these three steps have relatively moderate reaction kinetics, large quantities of LiPSs in the electrolyte cause an increased electrolyte concentration, and further lead to a raised internal resistance and polarization of the Li–S batteries. In addition, the dissolved LiPSs in the electrolyte will corrode the Li metal and form the insoluble Li_2S_2/Li_2S on the Li surface. An enhanced reaction kinetics can effectively shorten the detention time of the soluble LiPSs in the cathode, thereby suppressing the dissolution of LiPSs and decreasing the loss of active materials (Figure 1b).[7,18]

The last two steps are related to the reduction of high-order LiPSs to solid Li_2S_2/Li_2S. These conversions are much more difficult due to the crystallization of ionically/electrically insulating Li_2S_2.[19] The sluggish reaction kinetics in these steps leads to low sulfur utilization and limited discharge capacity (since these steps contribute about 75% specific capacity), thus the reversible specific capacity is strongly related to the reaction kinetics. Upon charging, the ionically/electrically insulating Li_2S_2/Li_2S on the cathode surface is difficult to convert to the soluble LiPSs, due to the high activation energy needed to overcome the nucleation barrier of solid Li_2S_2/Li_2S. The irreversible conversion of Li_2S_2/Li_2S further reduces the utilization of the active materials for both cathode and anode, and finally results in the dramatical capacity decay.

Although polar host materials can adsorb the LiPSs, they only mitigate the shuttle effect to some extent. The limited active adsorption sites of the polar materials are difficult to capture the continuously generated LiPSs, leading to the saturation of LiPSs. Moreover, the utilization of sulfur and the redox reaction kinetics of LiPSs are yet to be improved by these polar adsorbents.[20] The catalytic materials, in contrast, do not only capture the LiPSs with their active sites, but also enhance the redox reaction kinetics by accelerating the ion/electron transport.

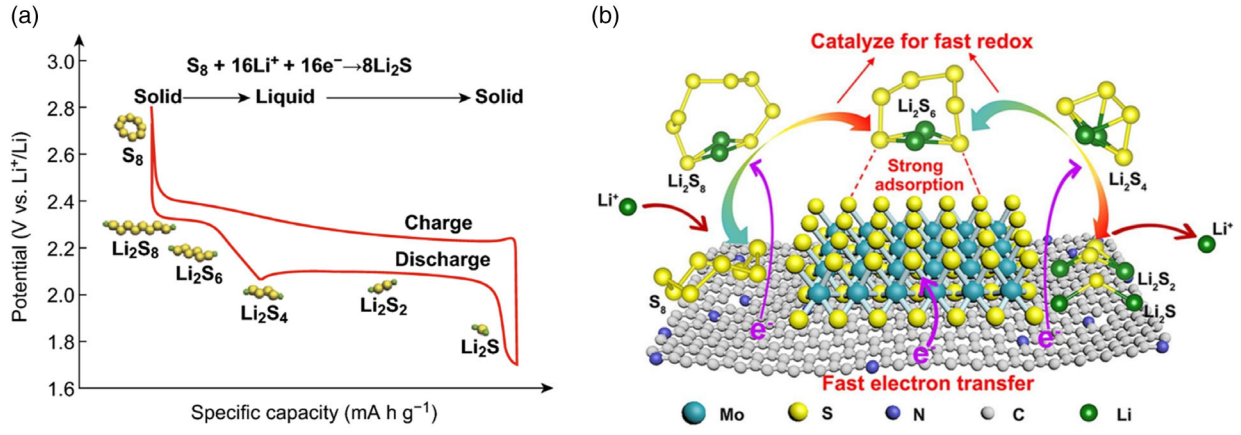

Figure 1. a) The typical charge/discharge profiles for Li–S batteries. Reproduced with permission.[17c] Copyright 2017, Wiley-VCH. b) Schematic illustration of nitrogen-doped CNT/MoS_2 nanosheets architecture for chemically immobilizing LiPSs and catalyzing the conversion of lithium polysulfides (LiPSs). Reproduced with permission.[18] Copyright 2019, The Royal Society of Chemistry.

Especially, the conversion rate between the soluble LiPSs and the insoluble Li_2S_2/Li_2S can be enhanced. Thereby, the catalytic materials can effectively alleviate the shuttle effect and improve the utilization of active sulfur.

To date, a variety of catalytic materials have been developed for Li–S batteries, including metal-free materials and metal-based materials.[15a,e,21] Metal-free catalytic materials are promising for Li–S batteries due to their low cost and light weight, which are beneficial for gravimetric energy density. Typically, N-doped carbon was reported as a Lewis base catalyst, the lone pair electrons of pyridinic and pyrrolic N have strong interactions with LiPSs and can accelerate the conversion of LiPSs.[22] Carbon nitrides are used for Li–S batteries owing to their chemical stability and unique structure, such as the graphitic carbon nitride ($g\text{-}C_3N_4$).[23] Black phosphorous is another metal-free catalytic material for Li–S batteries, because of its low resistivity, high room-temperature hole mobility, good conductivity, and high binding energies with LiPSs, which can chemically bind LiPSs and convert them to Li_2S.[24] Compared to metal-free catalytic materials, metal-based catalytic materials have higher electron conductivity and unique electronic properties, which can effectively inhibit the shuttle effect and prolong the electrochemical performance. The noble metal Pt coated on the Al foil current collector was used as electrocatalytic for Li–S batteries for the first time,[25] besides, non-noble metals Fe-, Co-, and Ni-based metal catalysts were also reported in Li–S batteries.[21b,26] Importantly, Fe-, Co-, and Ni-based single-atom catalysts (SACs) are well studied for Li–S batteries in recent years, SAC has unsaturated coordination environment, and atomic-level size which can realize the maximum exposure of the catalytic active sites with 100% utilization efficiency (in theoretical).[27] Moreover, transition metal compounds (M_aX_b, M: metal, X: anion) are one of the largest families of catalytic materials for Li–S batteries because of their unique physical/chemical properties depending on M and X, including oxides, sulfides, and nitrides[28] Interestingly, defect and heterostructure can regulate the properties of the catalytic materials and combine different materials as well as their merits, which are widely reported in both metal-free and metal-based catalytic materials.[29]

3. Molybdenum-Based Catalyst Materials for Advanced Li–S Batteries

Molybdenum is a transition metal with an atomic number of 42 and electronegativity of 2.16 on the Pauling scale.[30] In its pure form, Mo is a silvery-gray metal, and can form a variety of chemical compounds in oxidation states from −II to +IV.[30] Mo-bearing enzymes are by far the most common bacterial catalysts for breaking the chemical bond in atmospheric molecular nitrogen in the process of biological nitrogen fixation.[31] Mo-based compounds are also widely used in the electrochemical water splitting towards hydrogen evolution reaction (HER),[32] and have been considered as a promising alternative for HER due to their Pt-like activity and low cost.[33] Recently, Mo-based catalytic materials have been reported as highly efficient catalysts for advanced Li–S batteries (**Figure 2**).

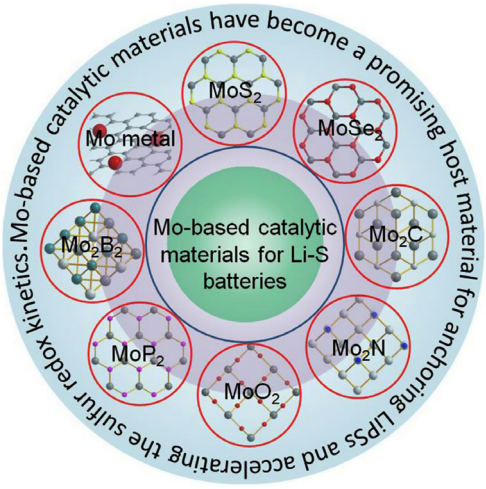

Figure 2. Varieties of Mo-based catalytic materials used for Li–S batteries, including Mo sulfides, diselenides, carbides, nitrides, oxides, phosphides, borides, and metal/single atoms/clusters.

3.1. Molybdenum Sulfides

3.1.1. MoS_2 Nanosheets

Arava and coworkers reported the catalytic effect of atomically thin monolayer/few-layer MoS_2.[34] Today, MoS_2-based composites have been widely studied as effective sulfur host materials for Li–S batteries, because of their highly efficient LiPSs catalytic activity.[35] Monolayer/few-layer MoS_2 nanosheets can be prepared by chemical vapor deposition (CVD) and shear-exfoliation methods at large scales. They facilitate electron transfer in the transformation reaction, which is initiated by the spatially localized adsorption of LiPSs by the unsaturated sulfur atoms at the edge sites (**Figure 3**a). Interestingly, the X-ray photoelectron spectroscopy (XPS) peaks related to the sulfate complexes are diminished after full discharge, accompanied by the increased intensity of short-chain LiPSs peaks and the slightly lowered binding energy.[34]

Ling and coworkers integrated few-layer MoS_2, active sulfur, and conductive reduced graphene oxide (rGO) into a hybrid sulfur cathode system (MoS_2/S/rGO). During the electrochemical process, MoS_2 nanosheets act as a multifunctional electrocatalyst. They can chemically adsorb LiPSs and, at the same time, kinetically accelerate the sulfur redox reactions.[36] With theoretical calculations, it is shown that MoS_2 nanosheets can reduce the Gibbs free energy for the rate-limiting step of sulfur reduction and the dissociation energy of Li_2S (Figure 3b).

When MHCS@MoS_2 (mesoporous hollow carbon sphere coated with MoS_2 nanosheets) is used as the sulfur host, the reduction of sulfur and the oxidation of Li_2S can be significantly accelerated, contributing to suppressed shuttle effect of LiPSs and prolonged lifespan. Thus, the MHCS@MoS_2/S cathode showed an ultralow capacity decay of 0.05% per cycle after 500 cycles at 1.0C.[37]

High-loading Li–S batteries using ultrathin MoS_2 nanosheets catalyst were also reported by Li and coworkers.[38] MoS_2 nanosheets were uniformly assembled in the carbon framework

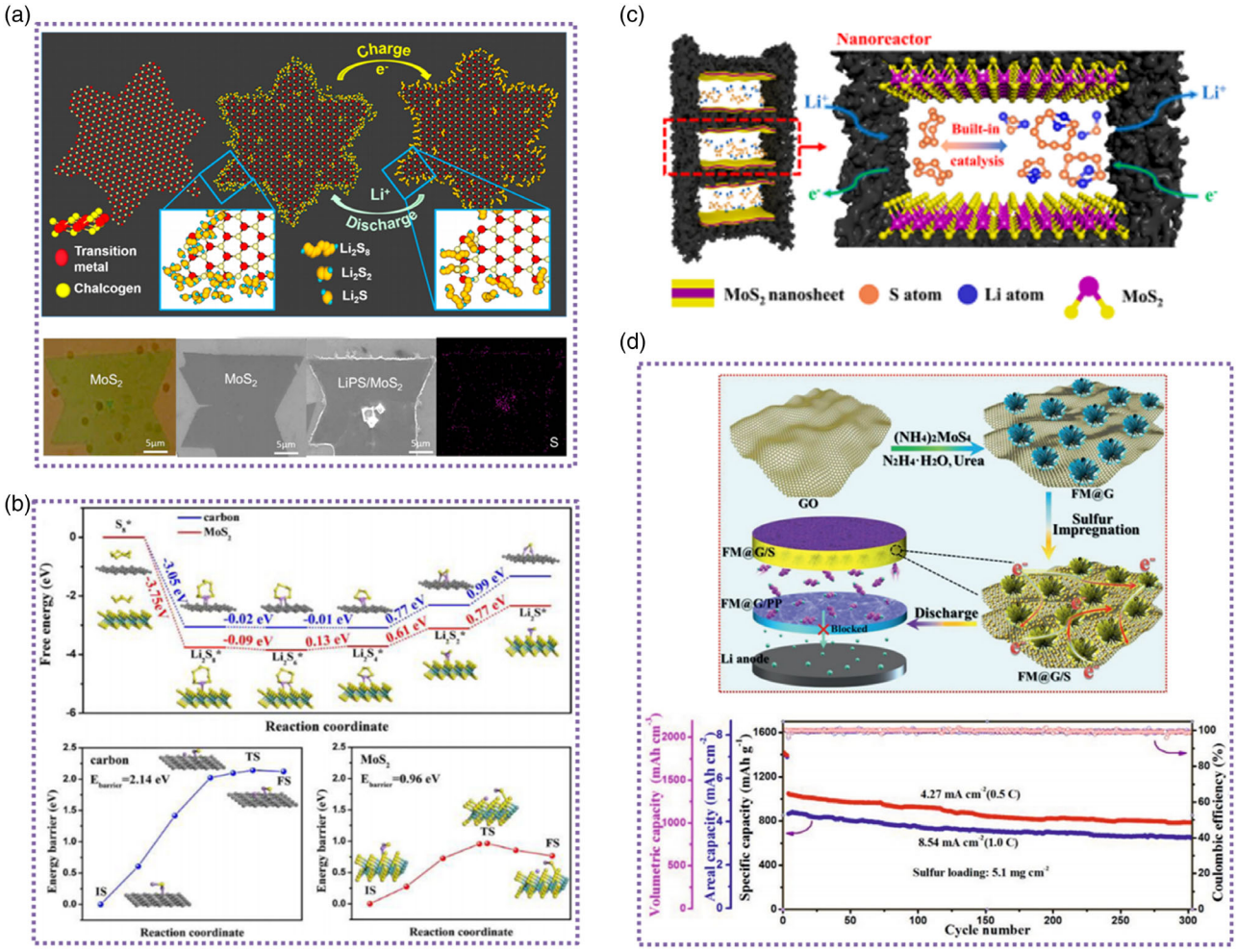

Figure 3. MoS_2 nanosheets used as effective sulfur host materials for Li–S batteries. a) Schematic illustration of transition metal dichalcogenide (MoS_2) nanosheets for Li−S battery, showing confined deposition of LiPSs at preferential catalytic sites and their conversions during discharge–charge processing. Optical and scanning electron microscope (SEM) images of MoS_2 flakes before and after deposition of LiPSs, and elemental mapping of sulfur. Reproduced with permission.[34] Copyright 2016, American Chemical Society. b) Energy profiles for the sulfur reduction on carbon and MoS_2 substrates, and energy profiles of the decomposition of Li_2S cluster. Reproduced with permission.[37] Copyright 2020, Elsevier. c) Illustration of confined nanoreactors in porous cavities between 2D (conductive) carbon layers with internal faces decorated by 2D (catalytic) MoS_2 nanosheets. Reproduced with permission.[38] Copyright 2020, American Chemical Society. d) Schematic illustration for the synthesis of FM@G and the systematic effect of a Li–S battery cycling performance at 0.5 and 1.0C. Reproduced with permission.[39] Copyright 2021, Wiley-VCH.

($C@MoS_2$). The good interface compatibility between the 2D conductive and catalytic building blocks enables a built-in catalytic conversion reaction in Li–S batteries (Figure 3c). This catalyst-in-conductor design enables a high sulfur loading of close to 80 wt%, and high capacity/cycling sustainability under a high sulfur loading of 6.0 mg cm^{-2}. Similarly, high sulfur mass loading and high volumetric capacity were achieved by Zhang and coworkers. They used the rGo decorated with metallic 1T-MoS_2 nanoflowers (FM@C) as the sulfur host. The S-deficient metallic MoS_2 nanoflowers in FM@G nanosheet process abundant accessible catalytic surface and fast electron transfer for chemical adsorption/catalytic conversion of LiPS. Thus, a high volumetric capacity of 1360 mAh cm^{-3} at 4.27 mA cm^{-2} was achieved in an ultrahigh sulfur mass loading up to 87 wt% (5.1 mg cm^{-2}) (Figure 3d).[39]

In addition, MoS_2 nanosheets are also widely used as separator coating materials or interlayers to suppress the shuttle effect through their chemical interactions with the LiPSs.[40] For example, Tang et al. prepared the flexible MoS_2/Celgard composite separator using the simple filtration method (**Figure 4**a).[41] When used as a separator in Li–S batteries, it can prevent LiPSs diffusion, thus significantly suppressing the LiPSs shuttling and yielding high Coulombic efficiency. Moreover, because of the excellent Li ion conductivity of the composite separator, it can facilitate the transport of Li ions and improve the lifespan and rate capability of Li–S batteries. Xie et al. fabricated a dual-functional separator coated by layer-by-layer self-assembled few-layer MoS_2 and polymer (Figure 4b).[42] When only coated 0.1 mg cm^{-2}, the Li–S batteries show excellent cycle stability with a negligible capacity decay of 0.029% per cycle over 2000 cycles at

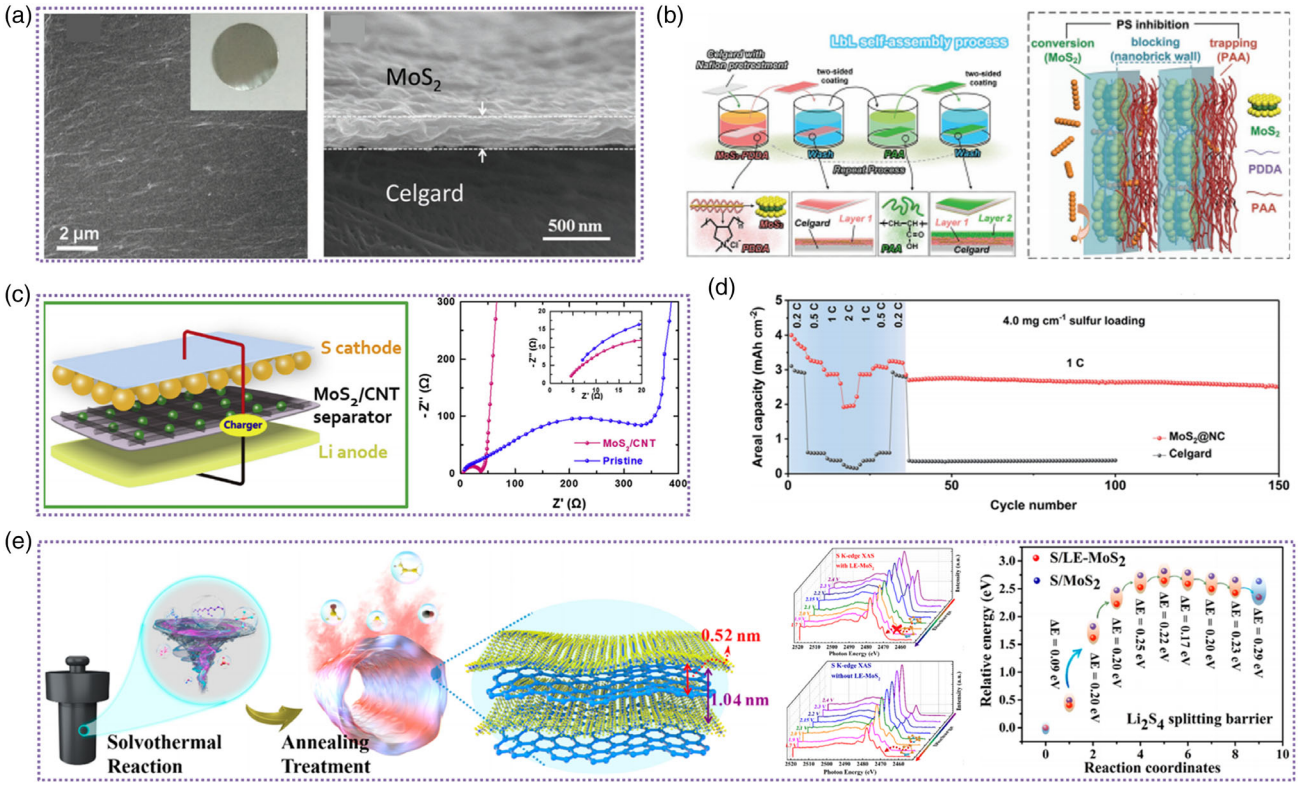

Figure 4. MoS_2 nanosheets used as separator coating materials or interlayers for Li–S batteries. a) SEM images of MoS_2/Celgard surface and cross-section of MoS_2 layers. Reproduced with permission.[40] Copyright 2017, Wiley-VCH. b) Schematic showing the layer-by-layer self-assembly process of MoS_2-polymer modified separator for Li–S battery. Reproduced with permission.[42] Copyright 2018, Wiley-VCH. c) Schematic diagram of a Li–S cell with the MoS_2/CNT interlayer, electrochemical impedance spectroscopy (EIS) spectra of the fresh cells with the MoS_2/CNT-interlayer-coated separator and pristine separator. Reproduced with permission.[44] Copyright 2018, Elsevier. d) Rate performance measured from 0.2 to 2C and the cycling stability at 1C after the step-wise rate performance at an increased sulfur loading of 4.0 mg cm^{-2} with MoS_2 nanosheet@N-doped carbon interlayer. Reproduced with permission.[45] Copyright 2019, The Royal Society of Chemistry 2019. e) Schematic illustration of LE-MoS_2 preparation and its enlarged interlayer. Sulfur K-edge X-ray absorption near edge structure with and without S/LE-MoS_2 electrode, splitting energy profiles for the transition from Li_2S_4 to Li_2S. Reproduced with permission.[46] Copyright 2020, American Chemical Society.

1C, an enhanced rate capability of 766 mAh g^{-1} at 3C, and a large reversible areal capability of 2.0 mAh cm^{-1} at 1C over 400 cycles.

To further improve the electrical conductivity during the electrochemical process, MoS_2 nanosheets combined with highly conductive carbon composites were used as the interlayer for Li–S batteries.[43] Wang et al. developed MoS_2/carbon nanotubes (CNT) interlayer by uniformly loading nanosheets on a cross-stacked CNT film (Figure 4c).[44] The CNT film provided good electrical conductivity for the sulfur cathode and a supporting skeleton for the dispersion of MoS_2, which further suppressed the shuttle effect through their chemical interactions with the LiPSs. The MoS_2 nanosheets encapsulated by nitrogen-doped carbon (MoS_2/NC) are also used as the interlayer (Figure 4d).[45] The homogeneous core–shell design ensures the intimate contact between MoS_2 and carbon, providing a smooth flow of electrons through the entire interlayer system to accelerate the LiPSs conversion. Therefore, highly efficient LiPSs immobilization and fast LiPSs kinetics can be realized, leading to an outstanding cyclability over 1500 cycles (with only 0.034% fading per cycle), improved rate performance, and high areal capacities of up to 3.7 mAh cm^{-2}. Interestingly, Zhang et al. designed a layer-spacing-enlarged MoS_2 (LE-MoS_2) consisting of hierarchical superstructural nanosheets for Li–S batteries (Figure 4e). Due to the expanded (002) lattice plane of MoS_2, the catalytic effect on the LiPSs transformation kinetics and the immobilization effect are both enhanced, which were also proved by the in situ X-ray adsorption near-edge structure spectroscopy and first-principles calculation.[46] As a result, sulfur-loaded LE-MoS_2 shows a high initial capacity of 1550 mAh g^{-1}, a low capacity fade rate of 0.06% per cycle, and a long-term lifespan of up to 500 cycles at 1C.

3.1.2. MoS_2 Heterostructures

A heterojunction is an interface between two layers or regions of dissimilar semiconductors, and a heterostructure contains multiple heterojunctions. Inspired by the unique band structure and synergistic effect of the heterostructure, MoS_2-based heterostructures are widely used as a sulfur host in recent years.[47] Zeng et al. reported the in situ growth of MoS_2 on nitrogen, sulfur DCC crosslinked $BaMn_{0.9}Mg_{0.1}O_3$ perovskite particle (PrNP), and CNTs heterostructure (DCC@MoS_2/PrNP/CNTs) (**Figure 5**a).[48] The DCC@MoS_2/PrNP/CNTs heterostructure displays a perfect 3D interconnected e^-/Li^+ conductive

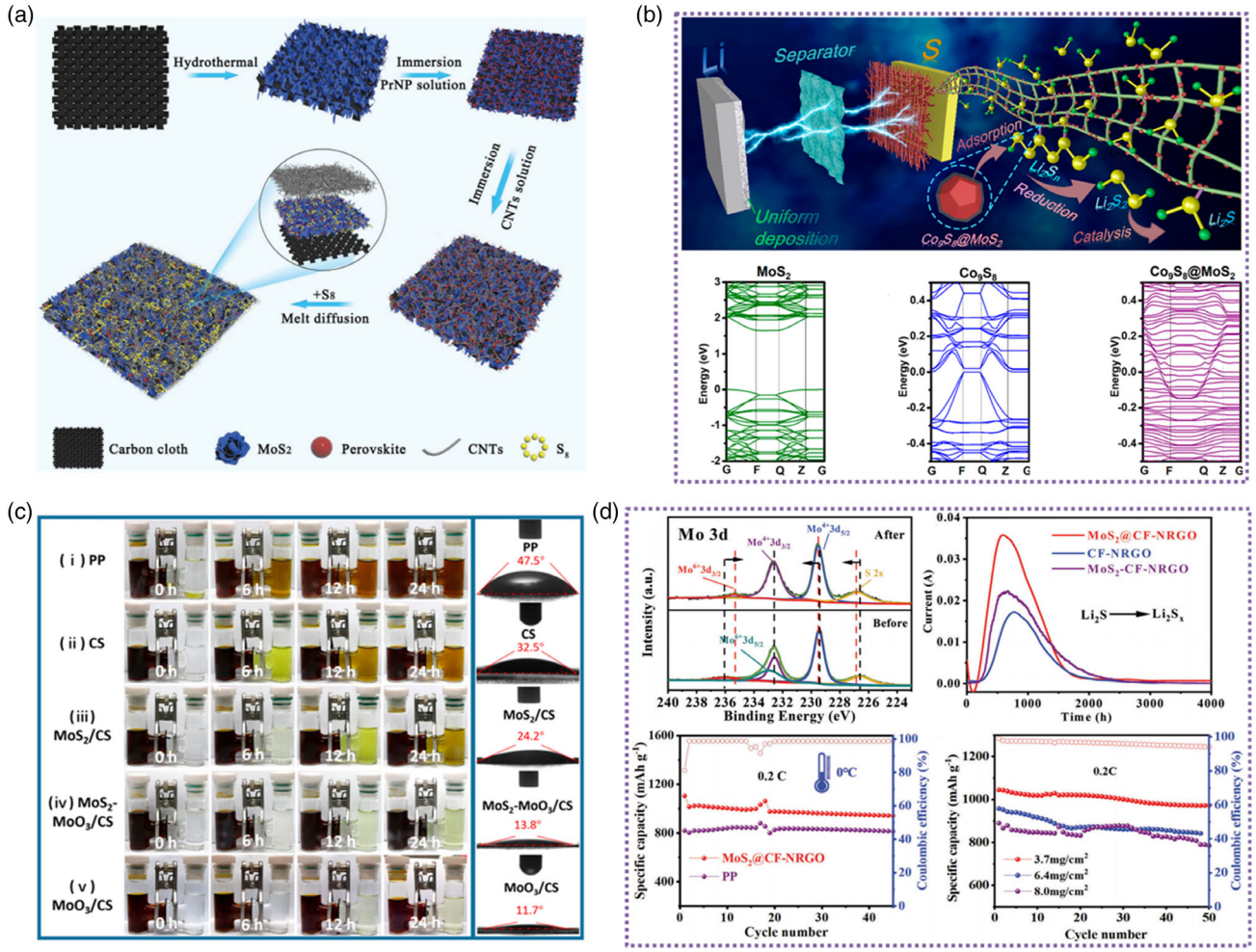

Figure 5. MoS_2-based heterostructures used as the sulfur host. a) Schematic illustration of the fabrication process of DCC@MoS_2/PrNP/CNTs/S electrode. Reproduced with permission.[48] Copyright 2018, Wiley-VCH. b) Schematic illustration of the Co_9S_8@MoS_2/CNF interlayer working in Li–S batteries, calculated band structures of MoS_2, Co_9S_8, and Co_9S_8@MoS_2. Reproduced with permission.[49] Copyright 2021, American Chemical Society. c) Polysulfide diffusion tests and the DME/DOL electrolyte contact angle shots of the PP, CS–PP, MoO_3/CS–PP, MoS_2/CS–PP, and MoS_2–MoO_3/CS–PP. Reproduced with permission.[50] Copyright 2020, American Chemical Society. d) XPS spectra of Mo 3*d* before and after adsorption with Li_2S_6, charge curves at 2.4 V of a Li_2S_8/tetraglyme solution on different the surfaces, cycling performance under 0 °C, and with high sulfur content. Reproduced with permission.[51] Copyright 2022, Wiley-VCH.

framework and a cooperative interface from amphipathicity sites synergistically bonded with the bipolar head of LiPSs. This structure stimulates the efficient immobilization and rapid conversion of LiPSs. Even with a high sulfur loading of 5.2 mg cm^{-2}, the heterostructure electrode still provides a high initial capacity of 882.7 mAh g^{-1} and an areal capacity of 4.75 mAh cm^{-2} after 50 cycles at 0.2C.

Xu et al. synthesized atomic-scale Co_9S_8@MoS_2 core–shell heterostructure-embedded carbon nanofiber (CNF) (Co_9S_8@MoS_2/CNF). The core–shell heterostructure modifies the band structure of MoS_2 (Figure 5b) and hence its electrical conductivity, leading to the enhancement of the chemical adsorption of LiPSs and the catalytic conversion of LiPSs to Li_2S.[49] As a result, the assembled Li–S batteries demonstrated a high discharge specific capacity of 477 mAh g^{-1} at a high current density of 5C. And even with high sulfur loadings of 6 and 10 mg cm^{-2}, high capacities of 1002 and 986 mAh g^{-1} can be obtained after 50 cycles, respectively. Zhang et al. synthesized the MoS_2–MoO_3 heterostructure and modified the separator for Li–S batteries.[50] These heterostructures can provide high surface area and strong polar surface affinity for trapping LiPSs (Figure 5c). Furthermore, the generated crystal distortions near the interface with more active sites could also promote the redox reaction of LiPSs. As a result, Li–S batteries with the MoS_2–MoO_3 heterostructure show a high initial discharge capacity of 1531 mAh g^{-1} at 0.2C, and only 0.0135% capacity decay per cycle after 600 cycles at 1C. Even at a high sulfur loading of 5.9 mg cm^{-2}, Li–S batteries still deliver a capacity of 640 mAh g^{-1} after 100 cycles at 0.2C.

MoS_2/nitrogen-doped reduced graphene oxide (MoS_2/C) heterogeneous interface can also significantly promote the transformation of LiPSs and decomposition of Li_2S.[51] The

XPS characteristic peaks of Mo^{6+} decreased in their intensities, and several Mo 3*d* peaks showed a slight shift after the adsorption of Li_2S_6, indicating a strong chemical reaction between Mo^{6+} and Li_2S_6. Moreover, compared with the other two electrodes (pure PP separator and nitrogen-doped reduced graphene oxide coated separator), the oxidation of solid Li_2S by MoS_2/C also exhibited a stronger enhancement, suggesting a significantly lower oxidation overpotential for Li_2S conversion (Figure 5d). Therefore, the cathode with MoS_2/C can deliver a high reversible capacity even at the low temperature of 0 °C, and an extremely high areal capacity of 6.11 mAh cm^{-2} can be achieved with high sulfur mass loading of 8.0 mg cm^{-2}.

3.1.3. Defect-Rich MoS_2

Defect engineering is an important strategy to regulate the atomic distribution and optimize the electronic structure of the nanomaterials, including vacancy and doping.[52] Very recently, defect engineering has been widely used in the modification of MoS_2-based hosts for Li–S batteries, which showed very motivating improvements in the electrochemical performances of these host materials. For instance, Yu et al. developed a 3D graphene aerogel (GA) decorated with defect-rich (vacancy) MoS_2 nanosheets (GA-DR-MoS_2) as a sulfur host (**Figure 6**a).[53] During the self-assembly process, the MoS_2 precursors were adsorbed by the functional groups of GO sheets, meanwhile, an excess of thiourea acts as a reductant for the Mo^{6+}–Mo^{4+} reaction. In addition, they also serve as an efficient additive for MoS_2 nanosheet defect manufacturing. Primary nanocrystallites adsorb excessive thiourea on their surface, thus partially impeding oriented crystal growth and forming a defect-rich structure. When used as an electrocatalyst for Li–S batteries, the defect-rich MoS_2 can significantly accelerate LiPSs redox kinetics during the electrochemical process owing to the

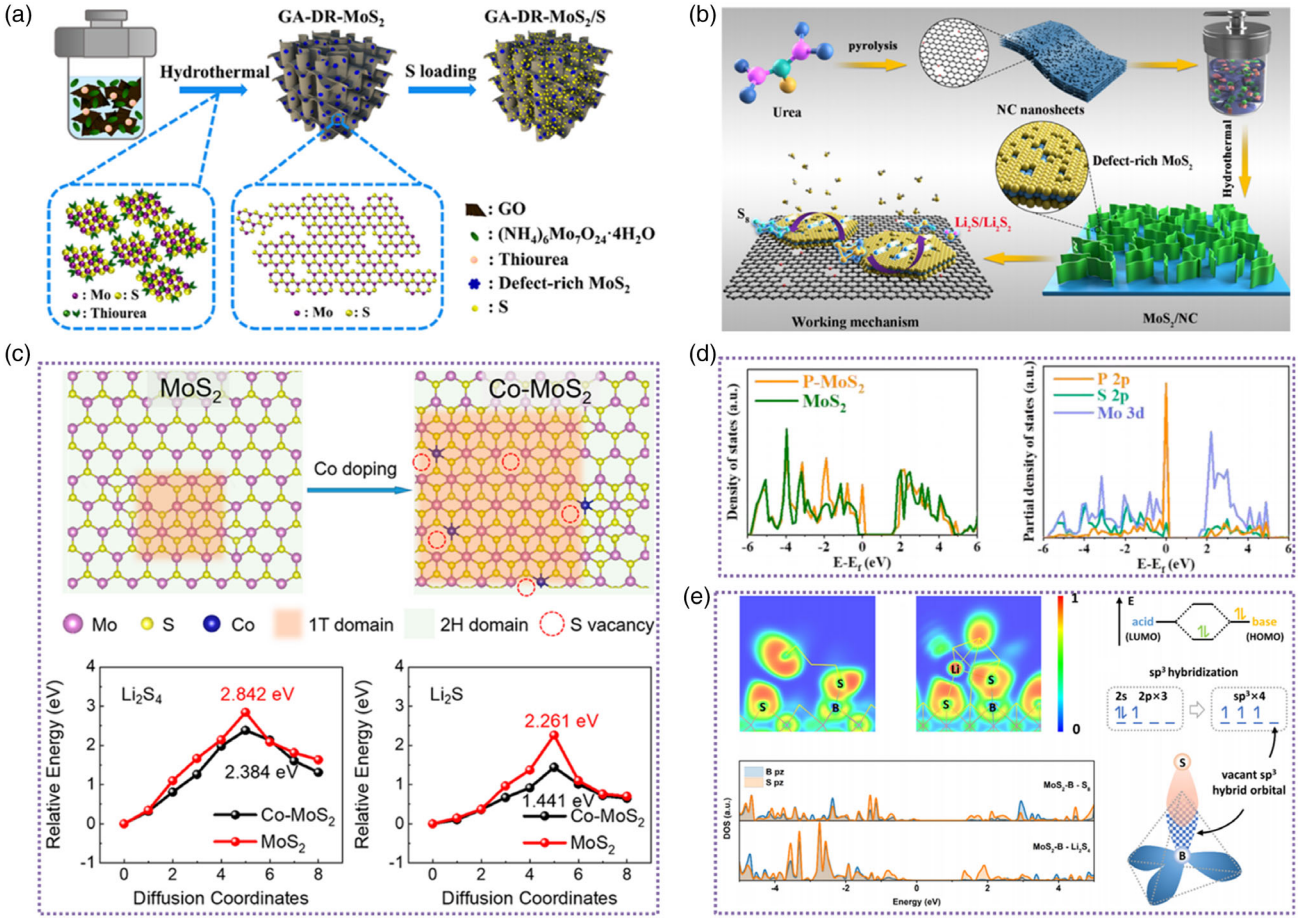

Figure 6. Defect-rich MoS_2 used for Li–S batteries. a) Schematic illustration of the GA-DR-MoS_2/S composite fabrication process. Reproduced with permission.[53] Copyright 2019, American Chemical Society. b) Schematic illustration of the defect-rich MoS_2/NC composite construction process and the working mechanism in Li–S batteries. Reproduced with permission.[54] Copyright 2020, American Chemical Society. c) Schematic of the structure and phase transition of MoS_2 after Co-doping, Li_2S_4 and Li_2S decomposition energies on 1T MoS_2 and 1T Co–MoS_2 monolayer. Reproduced with permission.[55] Copyright 2021, American Chemical Society. d) Density of states (DOS) plots for MoS_2 and P–MoS_2, and partial density of states (PDOS) results of P–MoS_2. Reproduced with permission.[56] Copyright 2021, Elsevier. e) Electron localization function (ELF) plots of the MoS_2–B–S_8 adsorption system and the MoS_2–B–Li_2S_4 adsorption system; schematic for Lewis acid–base interaction; DOS projected onto Pz orbitals for the MoS_2–B–S_8 adsorption system and the MoS_2–B–Li_2S_4 adsorption system; schematic for the sp^3 hybridization of B in MoS_2–B and the head-on orbital overlap between B and S. Reproduced with permission.[57] Copyright 2021, American Chemical Society.

enhanced exposure of active edge sites. Similarly, the defect-rich MoS_2/N-doped carbon nanosheets (MoS_2/NC) were synthesized by the aforementioned method (Shen et al. Figure 6b), and the obtained composite-coated PP (MoS_2/NC@PP) separator was used as a modified separator for Li–S batteries.[54] This modified separator demonstrated multifunctional effects: 1) the N-doped porous carbon nanosheets can be used as a conductive network to ensure fast electron transfer; 2) The defect-rich MoS_2 can not only effectively capture LiPSs and suppress the shuttle effect, but also offer abundant catalytic activity sites to enable fast redox reaction kinetics.

Heteroatom doping is another approach to tailor the electric conductivity, electronic configuration, and surface property of the nanomaterials, which can further tune the catalytic activity of the host materials for Li–S batteries. Lv et al. prepared a Co-doped MoS_2 (Co–MoS_2) through a hydrothermal method (Figure 6c), the density-functional theory (DFT) calculation suggests that the introduction of Co atoms can help to stabilize the 1T MoS_2, and the sulfur vacancy formation energy also decreases from 3.38 eV (2H MoS_2) to 1.92 eV (1T Co-doped MoS_2).[55] Moreover, The Li_2S_4, Li_2S_2, and Li_2S decomposition energies on 1T MoS_2 are 2.842, 2.403, and 2.261 eV, which decrease to 2.384, 1.529, and 1.441 eV after Co-doping, respectively, illustrating the 1T Co–MoS_2 has much better catalytic activity toward the redox reaction of LiPSs. In addition, non-metallic P element doping MoS_2 (P–MoS_2) was reported to modify the separator by Zhao et al. (Figure 6d),[56] from the DFT calculation, the electronic states and new defect levels occur in P–MoS_2 compared to that of the pristine MoS_2 at the Fermi level. And the partial density of states (PDOS) reveals that the P 2*p* orbital has strong hybridization with its neighboring Mo 3*d* orbital and S 2*p* orbital at the Fermi level. These results show that the introduction of P doped in MoS_2 leads to more charge transfers and increases the conductivity of MoS_2. In addition, the bond length of Li–S on the surface of P–MoS_2 is also the longest compared with MoS_2 and pristine Li_2S during the charging process, (2.399, 2.270, and 2.099 Å, respectively). A longer bond length helps to weaken the bond between atoms, thereby promoting the conversion of LiPSs and accelerating the redox kinetics.

Interestingly, B-doping was reported by Zhao et al. to tune the orbital orientation of MoS_2.[57] From the electron localization function (ELF) analysis, there are two electron localized areas around each S atom in S_8 (Figure 6e), which represent the two lone pairs of electrons, and one lone pair of electrons is used to form B–S coordinate link between MoS_2–B and S_8. In addition, MoS_2–B can also form B—S covalent bonding with Li_2S_4. The highest occupied molecular orbital (HOMO) of S (Lewis base) interacts with the lowest unoccupied molecular orbital (LUMO) of B (Lewis acid) to give a Lewis acid–base complex. Their interaction produces a coordinate covalent bond where S donates an electron pair to B. The DOS projected onto Pz orbitals for the MoS_2–B–S_8 and the MoS_2–B–Li_2S_4 adsorption systems. The significant electronic state overlap of Pz orbitals between B and S provides strong evidence for their intensive *z*-directional orbital coupling. The perpendicular orientation of the vacant orbital of B allows for maximal head-on overlap (σ bonding) with the occupied orbital of S to form a stable B—S bond. Thus, the basal plane of MoS_2 is efficiently activated; the CNT@MoS_2–B catalyst exhibits outstanding catalytic activity toward sulfur redox reactions, and achieves superior electrochemical performances for Li–S batteries.

For MoS_2, with its comparatively facile and controllable synthesis (of derivatives), including MoS_2 nanosheets, MoS_2 heterostructure, and defect-rich MoS_2, plenty of works suggest they can display enhanced electrochemical interactions with LiPSs, which are greatly promoting the catalytic materials for Li–S batteries. However, there is still room to further improve the activity of MoS_2 catalysts, for instance, 1) downsizing and maximizing the number of active sites; 2) using the few-layer or even single-layer MoS_2 nanosheets; 3) improving the intrinsic activity by tuning the electronic structure.

3.2. Molybdenum Diselenides/Tellurides

As isomorphic to MoS_2, the bandgap reduces when the chalcogen changes from S to Te, and the total density of states in the vicinity of the Fermi level for $MoSe_2$ and $MoTe_2$, conforming their metallic character and higher conductivity than MoS_2, which will potentially promote faster electrocatalyst activity to LiPSs, even though they have attracted much less attention than MoS_2 so far. Zhang et al. integrated $MoSe_2$ nanoflakes with carbon nanotube, and coated them on the PP separator for Li–S batteries ($MoSe_2$/CNT-PP) (**Figure 7**a).[58] Due to the polar nature of the $MoSe_2$ nanoflakes, strong chemisorption can be provided for LiPSs, and the CNTs can work as a charge transport channel. Li–S batteries with $MoSe_2$/CNT–PP separator deliver higher initial capacity, much better rate performance and cycling stability.

Moreover, $MoSe_2$-based heterostructure and heteroatom doping were also investigated as sulfur hosts. For example, Liu et al. prepared the $MoSe_2$@FC@Mo_2C heterostructure in which transition metal $MoSe_2$ and metallic Mo_2C are encapsulated into hollow fluorine co-doped carbon materials (Figure 7b).[59] Interestingly, when the $MoSe_2$@FC@Mo_2C heterostructure was used for Li–S batteries, the $MoSe_2$, Mo_2C, and FC demonstrated synergistic electrocatalysis activity, and the polar FC with strong electronegativity tend to promote the conversion of long-chain ($S_8 \leftrightarrow Li_2S_4$), while the polar $MoSe_2$ and Mo_2C with enriched oxygen vacancies accelerate the short-chain conversion ($Li_2S_4 \leftrightarrow Li_2S$). Thus, leading to fast redox kinetics of LiPSs, and displaying good performance even under a high sulfur contenting of 5.5 mg cm^{-2} and a lean E/S ratio of 5 mL g^{-1}. Similarly, Zhang et al. synthesized the $MoSe_2$/MoO_2 heterostructure by water-steam etching and used as the sulfur host (Figure 7c).[60] The $MoSe_2$/MoO_2 heterostructure can accelerate ionic diffusion and enhance electrolyte accessibility due to the excellent conductivity of $MoSe_2$. Moreover, the synergistic catalytic behavior and efficient trapping and conversion of LiPSs can be realized by the formation of the heterostructure.

Li et al. designed a bifunctional electrocatalyst by the manipulation of cation cobalt doping into $MoSe_2$ (Co–$MoSe_2$), which is in situ hybridized with conductive MXene nanosheets via a one-step hydrothermal reaction. In this design, cobalt doping is used to tailor the electronic structure and reactive sites of $MoSe_2$ to enhance the intrinsic catalytic activity and conductivity of $MoSe_2$.[61] From the cyclic voltammetry (CV) of symmetric cells, a higher current density was displayed for Co–$MoSe_2$/MXene (1.8 A g^{-1}) compared to that of pure $MoSe_2$/MXene

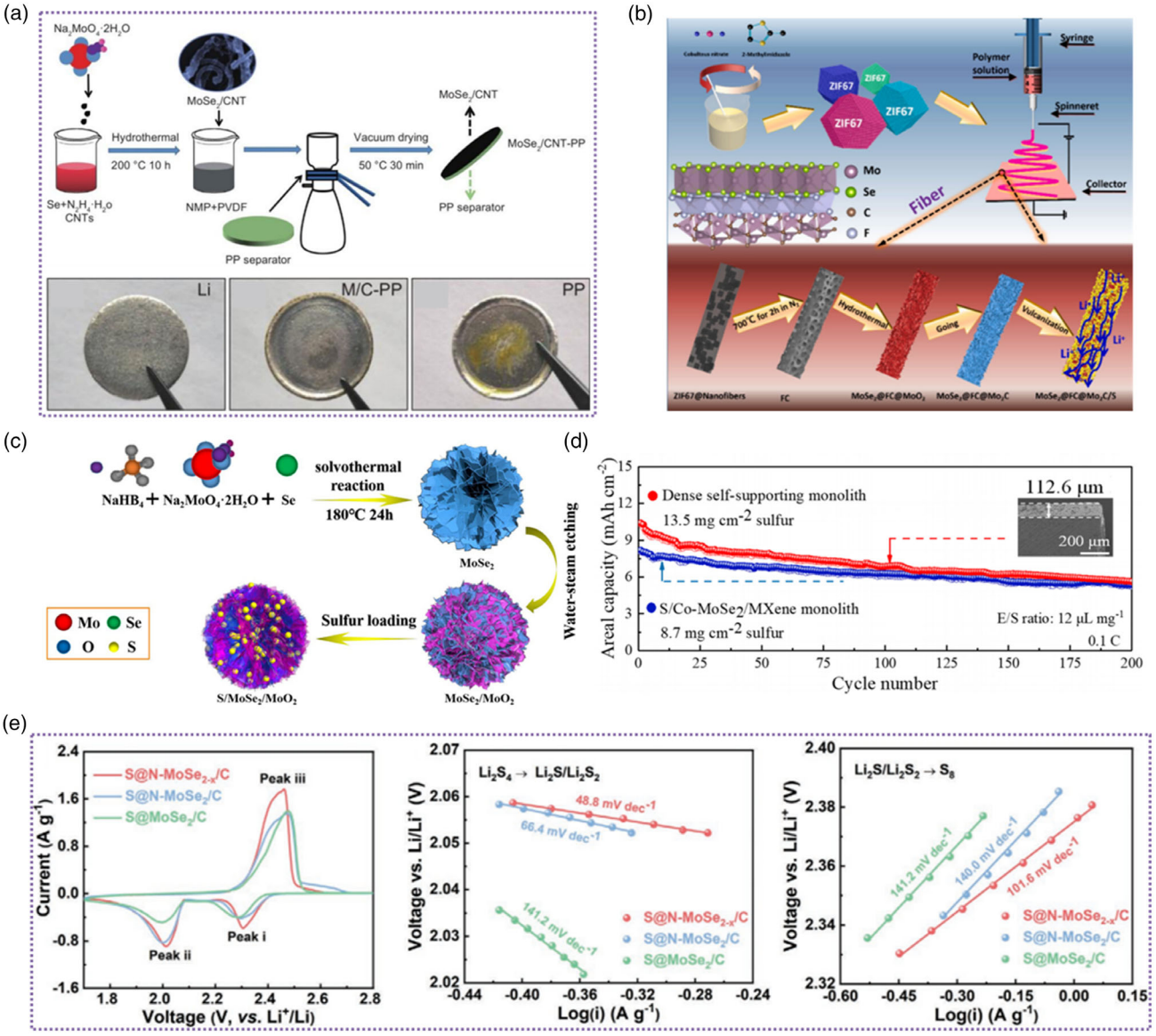

Figure 7. $MoSe_2/MoTe_2$ electrocatalyst used for Li–S batteries. a) The preparation process of $MoSe_2$/CNT–PP separator. Digital photos of Li foil, Li foil with M/C–PP, and Li foil with PP. Reproduced with permission.[58] Copyright 2021, Elsevier. b) The schematic diagram for the preparation of $MoSe_2$@FC@Mo_2C/S process. Reproduced with permission.[59] Copyright 2020, Elsevier. c) The schematic illustration of the synthesis process of S/$MoSe_2$/MoO_2 heterostructure. Reproduced with permission.[60] Copyright 2019, Elsevier. d) Areal capacities and cycling stability of a thick and dense monolith cathode and a dense self–supporting monolith cathode at 0.1C. Reproduced with permission.[61] Copyright 2021, American Chemical Society. e) CV profiles of S@N–$MoSe_{2-x}$/C, S@N–$MoSe_2$/C, and S@$MoSe_2$/C electrodes at a scan rate of 0.05 mV s^{-1}. Tafel plots of peak ii and peak iii. Reproduced with permission.[62] Copyright 2021, Wiley-VCH.

(1.25 A g^{-1}), suggesting that the catalytic conversion ability was significantly improved after Co doping. Impressively, even with the resultant dense S/Co–$MoSe_2$/MXene monolith cathode (13.5 mg cm^{-2}), the Li–S battery still delivered a high initial gravimetric capacity of 1454 mAh g^{-1} and an ultrahigh volumetric energy density of 3659 Wh L^{-1} at 0.1C (Figure 7d). Sun et al. proposed the introduction of N-doping (D_N) and Se-vacancies (V_{Se}) in the $MoSe_2$ electrocatalyst for sulfur chemistry.[62] The CV profiles reveal that the S@N–$MoSe_{2-x}$/C electrode displayed the largest current response and the lowest reaction polarization for all redox peaks, suggesting expedited sulfur redox kinetics originating from dual-defect engineering. Importantly, D_N significantly decreased the Tafel slope, while further incorporation of V_{Se} critically decreased. Since a smaller Tafel slope means a faster electrokinetic process, it could be corroborated that D_N and V_{Se} selectively accelerate the Li_2S nucleation and dissociation reactions, respectively (Figure 7e).

$MoTe_2$ with different phases (2H, 1T, and 1T') were investigated to prevent the shuttle effect for Li–S batteries, and the DFT calculations suggested that the 1T'-MoTe2 showed the

concentrated density of states (DOS) close to Fermi level with high conductivity.[63] Moreover, the in situ Raman spectroscopy revealed that the signals of high intensity of different mid- and long-chain (S_8^{2-}, S_6^{2-}, and S_4^{2-}) can be unmistakably distinguished from the time-resolved Raman image for the graphene/S cathode, while there are no obvious S_8^{2-}, S_6^{2-}, or S_4^{2-} Raman shifts noticed for the 1T′-$MoTe_2$ based cathode. Owing to the chemisorption and high catalytic effect of 1T′-$MoTe_2$, 1T′-$MoTe_2$ based cathode exhibits a highly reversible discharge capacity of 1310.1 mAh g^{-1} at 0.2C with 0.026% capacity fade rate per cycle over 600 cycles.

$MoSe_2$ and $MoTe_2$ have similar properties to MoS_2, the strategies to improve the activities for $MoSe_2$ and $MoTe_2$ can learn from MoS_2. However, the weight of $MoSe_2$ and $MoTe_2$ is much heavier than MoS_2, the weight ratio of catalytic materials in the cathode needs to be considered when used in Li–S batteries.

3.3. Molybdenum Carbides

Mo carbides (Mo_xC), with high conductivity, metallic characteristic, and superior catalytic effect are investigated as sulfur catalytic materials in recent years.[32,64] Liu et al. reported a uniform hollow structure constructed of double carbon shells and fully embedded polar metallic Mo_2C (Mo_2C/C@C) as the sulfur host.[65] Similarly, Lai et al. synthesized a hierarchical defective Mo_xC@N-doped carbon hollow microsphere (Mo_xC@NC) used for Li–S batteries.[66] The hierarchical hollow structure can facilitate electrolyte infiltration and fast electron/ion transportation, and buffer the volumetric expansion during the electrochemical process. Moreover, the defective Mo_xC with enhanced electrochemical interaction with LiPSs (**Figure 8**a), thus, the S cathode with Mo_xC@NC catalyst delivered a favorable specific capacity of 982 mAh g^{-1} at 0.5C, and maintained over 400 cycles with a low-capacity fading rate of 0.14% per cycle.

Interestingly, Qi et al. reported a Ni-tipped CNTs-on-MoC porous pillar foundation (MoC@Ni−NCNT) hierarchical nanoreactor with multiadsorption-catalytic sites produced by the CVD process (Figure 8b).[67] First, the dicyandiamide released the volatile CN_x gas when the calcination temperature reached at 600 °C, which is trapped by $NiMoO_4$ nanorods, triggering the exsolution of Ni nanoparticles and promoting the $NiMoO_4$ transformed into Ni/MoO_x to form MoN. Finally, the MoN converted to the MoC with a large number of nanoscale pores when the temperature reached 800 °C. Benefiting from these favorable features, even under a high sulfur loading of 6 mg cm^{-2}, Li–S batteries with MoC@Ni−NCNT catalyst can achieve a large areal capacity of 6.1 mAh cm^{-2} at 0.5C.

Since the small size of catalysts will provide more active sites, many efforts have been devoted to optimizing the

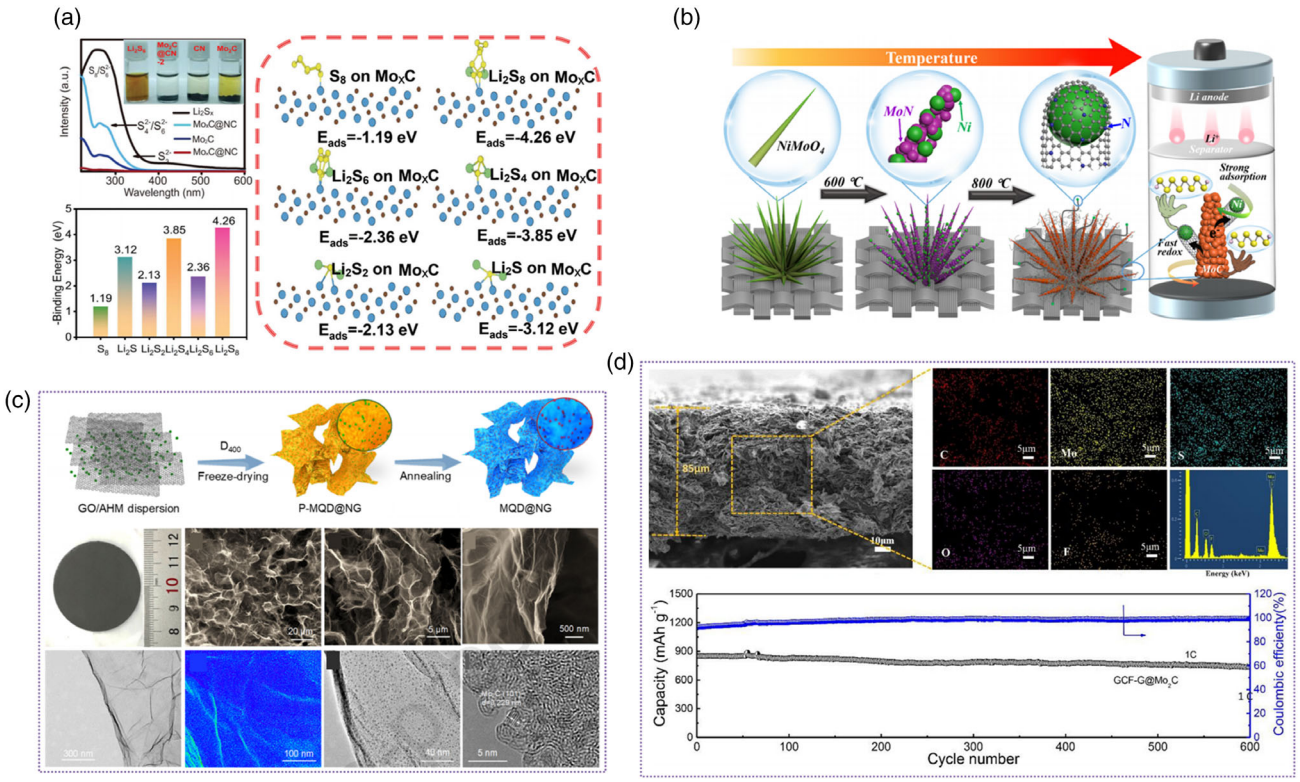

Figure 8. MoC_x-based electrocatalyst used for Li–S batteries. a) Enhanced electrochemical interaction between Mo_xC and LiPSs. Reproduced with permission.[66] Copyright 2022, The Royal Society of Chemistry. b) Schematic illustration of the direct chemical vapor deposition (CVD) fabrication of MoC@Ni−NCNT on the CFC substrate. Reproduced with permission from .[67] Copyright 2021, American Chemical Society. c) The Mo_2C quantum dots homogeneously anchor on graphene nanosheets. Reproduced with permission from .[69] Copyright 2020, Elsevier. d) SEM image and corresponding elemental maps of S, Mo, C, O and F, EDS spectra after 50 cycles, and long-term cycling performance at the rate of 1C for 600 cycles. Reproduced with permission.[74] Copyright 2020, Elsevier.

size/morphology of the Mo_xC-based catalysts.[68] He et al. reported a novel Mo_2C quantum dots@graphene functionalized separator for Li–S batteries.[69] The precursor gel of Mo_2C quantum dots (QDs) anchored N-doped graphene (NG) nanosheets (P-MQD@NG) was synthesized by hydrothermal method, then $(NH_4)_6Mo_7O_{24}{\cdot}4H_2O$ and poly(oxypropylene) diamines (D400) was dissolved into graphene oxide solution, the P-MQD@NG was obtained when heating the solution at 90 °C. After freeze-drying, the MQD@NG can be obtained by annealing in an Ar atmosphere. Significantly, the high-resolution transmission electron microscopy (HRTEM) image strongly supports the Mo_2C quantum dots homogeneously anchor on graphene nanosheets, and have a uniform morphology with an average diameter of only 1.8 nm (Figure 8c). Liu et al. prepared the ultrafine Mo_2C nanocrystallites encapsulated in porous carbon substrate (Mo_2C–CNOs) via a MOFs-assisted strategy.[70] When used as the sulfur host for Li–S batteries, the highly polar Mo_2C can chemically adsorb the LiPSs due to the formation of a strong Mo—S bond. Besides, the Mo_2C nanoparticles with enhanced electrocatalytic activity can boost the redox reaction kinetics of sulfur species during the electrochemical process. As a result, even with a high sulfur content of 72.15 wt%, the S cathode with Mo_2C–CNOs catalyst can deliver a favorable specific capacity of 1396 mAh g^{-1} at 0.1C. Similarly, Li et al. reported the Ketjenblack matrix decorated with ultra-small Mo_2C nanoparticles (KB/US-Mo_2C) by "in situ growth" strategy, and coated on the PP separator for Li–S batteries.[71]

Compared to the traditional S cathode slurry coating process, S electrodes with a freestanding structure can avoid the inactive components, such as, binders, conductive agents, and aluminium current collectors, thus, improving the energy density of the Li–S batteries.[72] Lu et al. fabricated freestanding Mo_2C-decorated N-doping carbon nanofibers (Mo_2C-NCNFs) as a 3D current collector for Li–S batteries. This interconnected 3D nanofibers structure guarantees structural integrity, excellent electronic transport, and fast electrochemical reaction kinetics.[73] Cheng et al. reported the graphene@Mo_2C nanoparticles (GCF-G@Mo_2C) heterostructure supported by lightweight graphitic carbon foam as the freestanding S electrode for Li–S batteries (Figure 8d).[74] The N-doped carbon foam wrapped by graphene sheets with an agaric-like porous structure can achieve fast mass transport and electrolyte infiltration, and high S mass loading. When combined with Mo_2C electrocatalyst, it can afford effective anchoring/catalytic sites to LiPSs. As a result, this architecture of GCF-G@Mo_2C can accommodate extremely high sulfur loading up to 10.5 mg cm^{-2}, exceeding most of the previous Li–S works.

For Mo carbides, they show high conductivity, metallic characteristic, and enhanced catalytic effect for LiPSs, nevertheless, high-temperature conditions are required during the synthesis, and the well-defined crystalline phase is often difficult to obtain. Therefore, more controllable synthesis approaches with moderate temperatures should be developed for MoC_x catalysts.

3.4. Molybdenum Nitrides

Mo nitrides with a polar structure and high electrical conductivity have been widely investigated as the sulfur hosts for Li–S batteries.[75] Wang et al. reported the template-assisted fabrication of mesoporous and conductive Mo_2N with a high surface area of 121 m^2 g^{-1}, a pore size of 8.6 nm, and a conductivity of 1×10^5 S m^{-1} (**Figure 9**a). During the electrochemical process, conductive interwoven skeletons can speed up electron transport, and boost LiPSs redox conversion. In addition, mesoporous Mo_2N with a high surface area provides a high polar surface area for chemical binding LiPSs and efficient suppression shuttling effect.[76] Similarly, Sun et al. fabricated the MoN microrod using the one-pot ammoniation strategy of the metal–oxide template, even with a high areal loading of 3.1 mg cm^{-2}, the MoN–S cathode could deliver an initial discharge capacity of 1315 mAh g^{-1} and maintain a reversible capacity of 902 mAh g^{-1} after 350 cycles.[77] Liang et al. prepared thorn-like carbon nanofibers combined with MoN nanosheets (MoN@CNFs). Using the MoN as a multifunctional coating to modify conventional Celgard separators, Li–S batteries can achieve impressive performance because the MoN nanosheets can chemically anchor polysulfides and distinctly improve the redox kinetics of LiPSs (Figure 9b).[78]

The heterostructural mediators combining high conductivity and high polarity can accelerate the LiPSs conversion and regulate the deposition of solid Li_2S/Li_2S_2.[79] Recently, MoN/Mo_2N-based heterostructures were reported for Li–S batteries, Cao et al. designed the MoO_2–Mo_2N nanobelts as the multifunctional interlayer for Li–S batteries (Figure 9c).[80] After interacting with Li_2S_6, the valence state of Mo from the MoO_2 sample showed slight binding energy shifts around −0.5–−0.8 eV, which indicates the electron exchange between Li_2S_6. And a new peak around 529.48 eV in MoO_2–Li_2S_6 represents the formation of Li–O binding after the chemisorption to Li_2S_6 species and MoO_2. Similarly, a certain amount of Mo^{6+} in Mo_2N was reduced and the peaks of both Mo^{4+}, Mo^{5+}, and $Mo^{\delta+}$ shifted to lower binding energy owing to the increased electron density at the metal center. And a negative shift of the Mo–N peak (from 394.82 to 394.19 eV) also indicates the interaction between Li-ion and N atom. These XPS results demonstrate that the MoO_2–Mo_2N binary structure can sufficiently restrict the shuttling of LiPSs and prompt the conversion kinetics. Sun et al. designed the MoS_2–MoN heterostructure nanosheets as sulfur hosts.[81] From the hard X-ray micro-analysis (HXMA), the Mo pre-edge in the MoS_2 host moves slightly to a lower energy position. On the contrary, the Mo pre-edges in MoS_2–MoN and MoN hosts shift to higher energy positions, indicating that the valance of Mo ions ascends after reaction with Li_2S_6.[82] Because of their respective advantages, LiPSs trapping ability and fast surface Li^+ diffusion (by MoS_2) as well as high electron conductivity and coupled electron transfer through redox reaction (by MoN) for LiPS conversion, the MoS_2–MoN host could show high areal capacity even with ultrahigh loadings of 12.2 mg cm^{-2} (sulfur content of 72.7%) and lean electrolyte usage down to 4.2 mL g^{-1}.

Mo nitrides have high conductivity, polar structure, and enhanced catalytic properties, which can anchor LiPSs and accelerate sulfur redox kinetics. However, similar to Mo carbides, the synthesis of Mo nitrides generally needs high-temperature conditions and lack a facile synthesis approach.

3.5. Molybdenum Oxides

Mo oxides are a kind of polar metal oxides with high electronic conductivity, wide bandgap, and abundant oxygen vacancies,

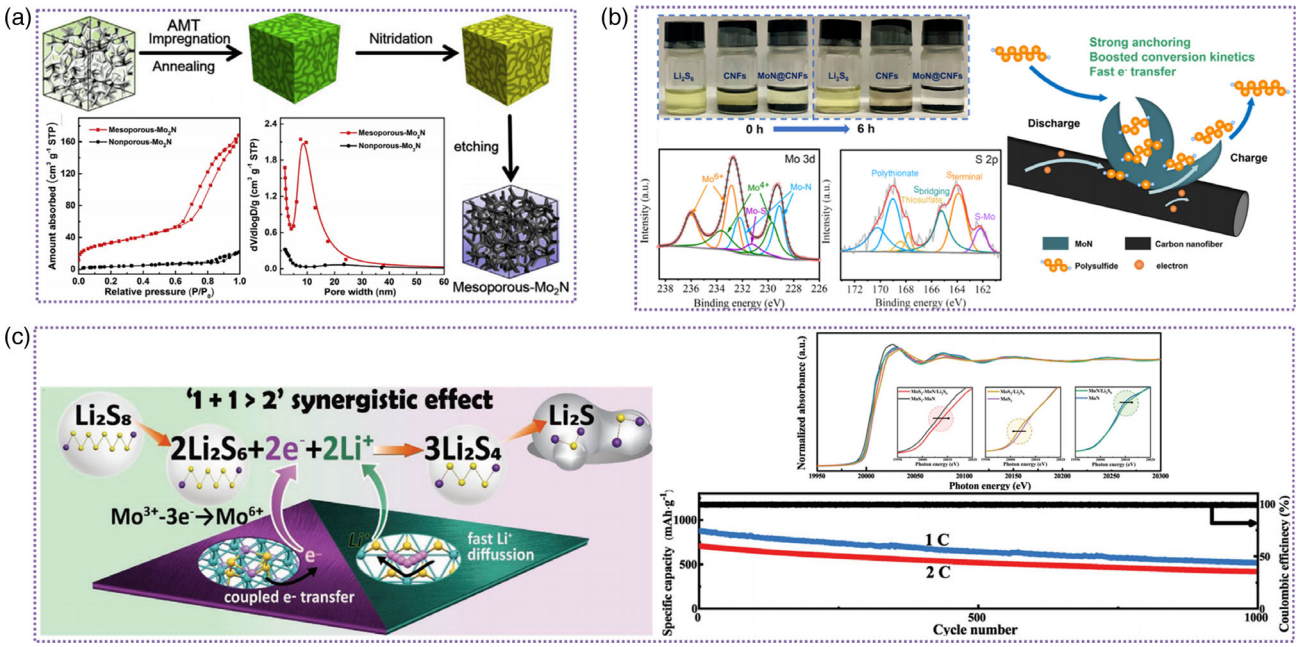

Figure 9. Mo nitrides used as sulfur host materials. a) Schematic illustration of the fabrication of mesoporous-Mo_2N. Reproduced with permission.[76] Copyright 2018, Elsevier. b) The LiPSs anchoring and enhanced conversion on the surface of exposed MoN nanosheets. Reproduced with permission.[78] Copyright 2022. American Chemical Society. c) The synergistic catalytic conversion of LiPSs by the MoS_2–MoN heterostructure, hard X-ray micro-analysis (HXMA) spectra of molybdenum K-edge before/after soaking in Li_2S_6 solutions, and long-term cycling performance. Reproduced with permission.[79] Copyright 2021, Wiley-VCH.

which exhibit versatile catalytic activities for many reactions.[83] Xiang et al. synthesized the reduced graphene oxide/molybdenum dioxide (rGO/MoO_2) composite to modify the PP separator for Li–S batteries.[84] The modified PP separator introduces physical adsorption, chemical anchoring, and catalytic effects to restrain the "shuttle effect", thus improving the electrochemical performances of Li–S batteries. MoO_3 nanoparticles[85] and MoO_3 spheres[86] were also used for Li–S batteries, the layer structure of MoO_3 with octahedral holes and extension channels, which can function as the embedding locations and diffusing channels for Li^+, and the oxygen atoms on the MoO_3 host can form the chemical binding interactions with LiPSs, thus alleviating the dissolution of the LiPSs (**Figure 10**a). In addition, Zhao et al. reported the growth of MoO_3 nanoflakes onto the carbon paper (MoO_3-CP), which served as an efficient cathode electrode for Li–S batteries.[87] Because the MoO_3 can offer a strong binding ability to anchor LiPSs at the electrode surface and exhibit extraordinary catalytic activity toward LiPSs redox reaction, even with a high sulfur loading of 8 mg cm^{-2}, the specific capacity retention rate of Li–S batteries can still keep as high as 68.75% after 1000 cycles at 1C (Figure 10b).

MoO_2-based heterostructures were also used for Li–S batteries, for instance, Manthiram et al. reported the in situ growth of the MoO_2/MoS_2 hybrid nanosheets onto the carbon cloth (MoO_2/MoS_2@CC),[88] the MoO_2/MoS_2 hybrid integrates the advantages of conductive MoO_2 and sulfiphilic MoS_2, which exhibits excellent catalytic effect, enhances charge transfer and greatly promotes the redox kinetics of LiPSs transformation. As shown in Figure 10c, the CV curves with MoO_2/MoS_2 nanosheets have much sharper peaks, lower polarization, and lower redox peak separation between cathodic and anodic peaks, illustrating the enhanced redox kinetics. Besides, the Nyquist plots revealed a lower resistance compared with the pure carbon paper, implying the great enhancement in charge transfer brought by MoO_2/MoS_2 nanosheets. The insulating Li_2S layer may lead to rapid passivation of the surface during the electrochemical process and result in poor reaction kinetics, thus impeding the subsequent Li_2S deposition and resulting the fast capacity decay. Cao et al. reported that the MoO_2/α-MoC heterostructure can influence the redox process of sulfur species and Li_2S deposition behavior.[89] The capacity of Li_2S is 160, 167, and 245 mAh g^{-1} when precipitation on MoO_2, α-MoC, and MoO_2/α-MoC, respectively, indicating that MoO_2/α-MoC is conducive to facilitating the liquid–solid phase transformation (Li_2S_4–Li_2S) during the electrochemical process (Figure 10d). Moreover, the oxidation response current of the MoO_2/α-MoC electrode is higher than MoO_2 and α-MoC electrodes, suggesting improved catalytic activity of the MoO_2/α-MoC heterostructure.

Polar Mo oxides with low cost, wide bandgap, and abundant oxygen vacancies on the surface, which exhibit versatile catalytic activities for LiPSs, while the electrical conductivity of Mo oxides is relatively low, the tuning of electron structure and/or introducing of conductive frameworks for Mo oxides are highly necessary.

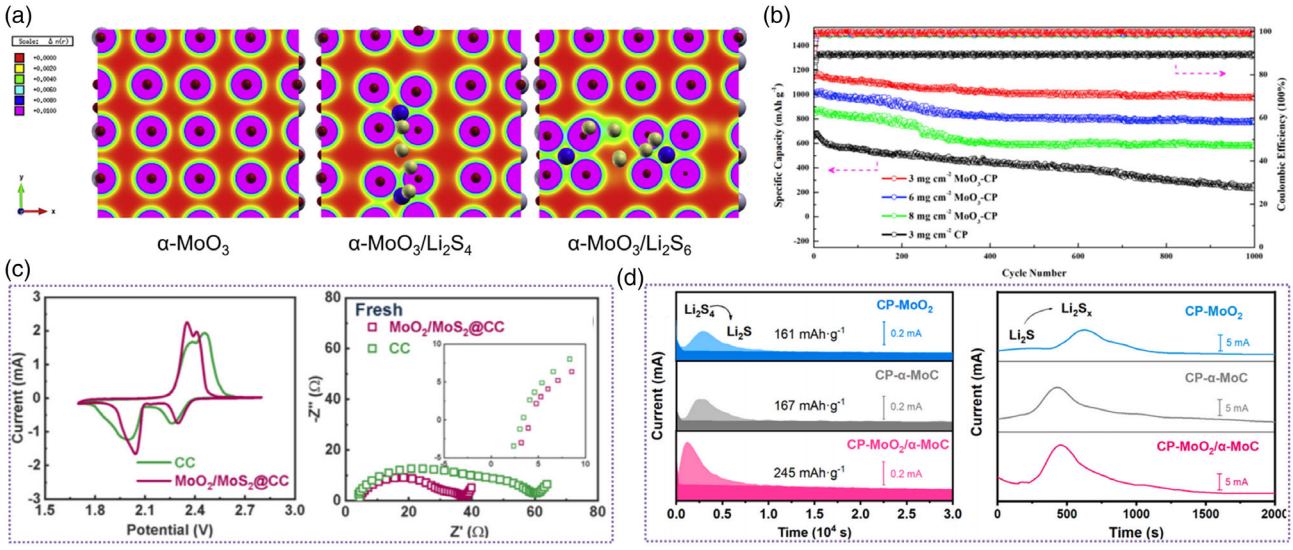

Figure 10. Mo oxides used for Li–S batteries. a) Charge density plots of pure α-MoO_3 c), α-MoO_3/Li_2S_4 d) and α-MoO_3/Li_2S_6. Reproduced with permission.[86] Copyright 2018, Elsevier. b) The cycling performance of Li–S batteries with MoO_3–CP and CP electrodes at the current densities of 1C. Reproduced with permission.[87] Copyright 2019, Elsevier. c) CV curves and EIS spectra of MoO_2/MoS_2@CC and pure carbon cloth. Reproduced with permission.[88] Copyright 2020, Elsevier. d) Potentiostatic discharge *i*–*t* profiles at 2.09 V on different samples, and potentiostatic charge *i*–*t* profiles at 2.40 V on different samples for evaluation of Li_2S dissolution behavior. Reproduced with permission.[89] Copyright 2021, Elsevier.

3.6. Other Mo-Based Compounds

Mo phosphides have high electron conductivity and strong interaction with LiPSs, which are investigated for Li–S batteries.[90] Li et al. synthesized the Ru-doped Mo_4P_3 nanoparticles and employed it as sulfur hosts (**Figure 11**a).[91] The Ru 3*p* XPS spectrum showed that a new peak observed at 482.6 eV can be assigned to the Ru—S bond after immersion with Li_2S_4, revealing the strong interaction of Ru with LiPS; at meaning while, the Mo $3d_{5/2}$ and $3d_{3/2}$ peaks of Mo 3*d* spectra shifted to the lower binding energy of 232.1 and 228.0 eV, reflecting the interaction of Mo with LiPSs. Thus, the Ru–Mo_4P_3 electrode delivered excellent rate capability with a capacity of 660 mAh g^{-1} at 4C, and a low-capacity decay of 0.07% per cycle at 3C even with a high S content of 77%. Moreover, Chen et al. reported the MoP quantum dots anchored to N, P-doped graphene (MPQ@G) as a highly efficient electrocatalyst for Li–S batteries (Figure 11b).[92] The MoP quantum dots possess a uniform morphology with an average diameter of ≈1.6 nm, which provided an abundance of the exposed active sites for LiPSs during the electrochemical process. In addition, due to the unique advantages of MoP and MoS_2, the MoP–MoS_2 heterostructure was also investigated to modify the PP separator for Li–S batteries (Figure 11c).[93] These flower-like heterostructures, composed of stacked nanosheets, provide numerous activity sites for LiPSs, thus promoting the reaction kinetics of LiPSs.

Recently, the anchoring and electrocatalysis of Mo borides were extensively studied for Li–S batteries by density functional theory,[94] as shown in Figure 11d, the catalytic performance on the discharge reactions was evaluated by calculating the Gibbs free energy diagrams of S_8 and a series LiPSs on $Mo_2B_2O_2$ and $Mo_2B_2F_2$. The reduction of S_8 to Li_2S_8 on both $Mo_2B_2O_2$ and $Mo_2B_2F_2$ is exothermic with remarkable energy downhills of 5.325 and 3.055 eV, respectively, suggesting fast kinetics. Moreover, the reduction from Li_2S_2 to Li_2S has an energy uphill of 0.744 eV on $Mo_2B_2F_2$, while the free energy has a favorable downhill of 0.322 eV on $Mo_2B_2O_2$, revealing the S atom of Li_2S is adsorbed on the surface of $Mo_2B_2O_2$. Besides, both $Mo_2B_2O_2$ and $Mo_2B_2F_2$ can significantly decrease the Li_2S decomposition barrier from 3.39 to 1.152/0.441 eV, respectively. This work provided a general design principle for improving the electrochemical performance of Mo borides for Li–S batteries.

Mo phosphides have similar metallic properties to Mo carbides, except that phosphorus (P) has a much lower electronegativity than that of carbon, which allows Mo phosphides to more efficiently catalyze LiPSs conversion. In turn, oxide coating more readily occurs on Mo phosphides surface than on Mo carbides, thus, surface protection for Mo phosphides catalytic materials should be considered.

3.7. Mo-Based Metal/Single Atoms/Cluster

Recently, our group prepared the monodisperse Mo nanoparticles with an average diameter of 1.24 nm (embedded onto nitrogen-doped graphene, Mo@N-G) and used as a highly efficient catalyst for Li–S batteries (**Figure 12**a).[95] During the electrochemical process, the unfilled d orbitals of oxidized Mo can attract electrons from the LiPS anions and form the Mo—S bond, thus promoting the conversion of LiPSs. Importantly, even with only 9% catalyst, the Li–S batteries can exhibit a large initial discharge capacity of 1359 mAh g^{-1}, superior cycling stability with 92.7% capacity retention over 100 cycles, and enhanced reaction kinetics under large current densities (676 mAh g^{-1}, 10C). Tan et al. fabricated a Mo–Li_2S–graphene capsule, where Mo nanocrystal catalysts and graphene-encapsulated shells are

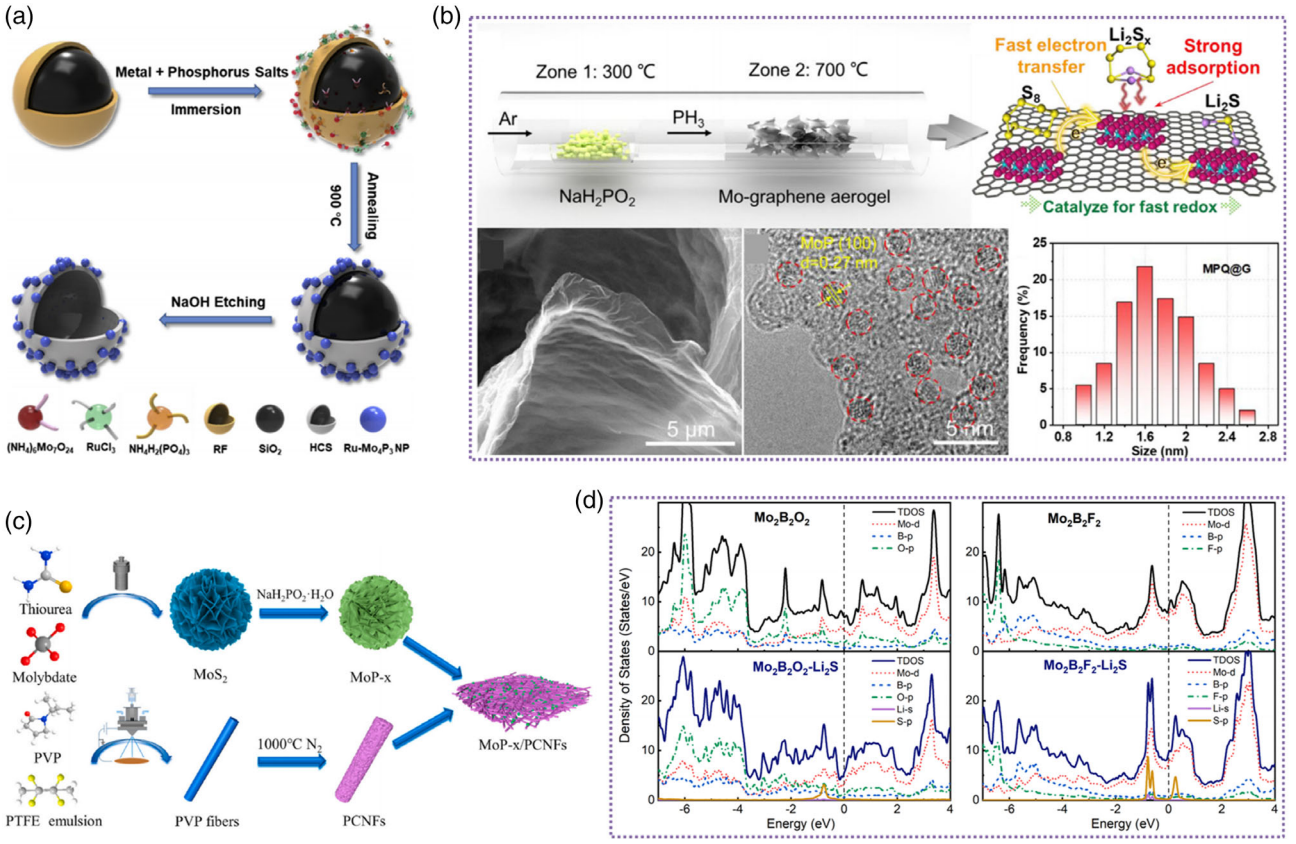

Figure 11. Mo phosphides and borides use for Li–S batteries. a) Schematic illustration of the preparation of the HCS–Ru–Mo_4P_3 NPs. Reproduced with permission.[91] Copyright 2019, Elsevier. b) Schematic of the synthetic procedure of the MPQ@G/S composite, catalytic mechanism, and the corresponding characterizations. Reproduced with permission.[92] Copyright 2021, Elsevier. c) Schematic illustration of the fabrication of MoP–x/PCNFs. Reproduced with permission.[93] Copyright 2021, Elsevier. d) Energy profiles for the S_8 and LiPSs reduction on $Mo_2B_2F_2$ (black line) and $Mo_2B_2O_2$ (red line) substrates. Reproduced with permission.[94] Copyright 2021, Elsevier.

produced simultaneously with the nucleation of crystalline Li_2S cores, achieving excellent electrochemical performance with high areal mass loading of 8.1 mg cm^{-2} for Li–S batteries.[96] More importantly, Mo–Li_2S–graphene can serve as a cathode material for a Li-metal-free Li-ion battery system when paired with Si/C anodes (Mo–Li_2S–graphene//Si–C full cell), as shown in Figure 12b, the full cell delivered high initial charge/discharge capacity of 880 and 608 mAh g^{-1}, which is almost twice that of the Li-rich cathode material. Besides, a high reversible capacity of 545 mAh g^{-1} (1C) with a capacity retention of 85.6% after 200 cycles was also achieved for the full cell. Furthermore, the single atoms Mo anchored in nitrogen-doped carbon nanoflowers (Mo–N–C–CNF) were also reported as sulfur hosts for Li–S batteries.[97] The high content of N_4-coordinated Mo atoms in multi-stage carbon sheets can optimize the hydrophilicity, Li-ion diffusion, LiPSs adsorption, and reaction kinetics.

In addition, Mo nanoclusters were also used as the host for Li–S batteries, for example, Sun et al. deposited metallic Mo on the surface of the CNT through the magnetron sputtering process (Figure 12c).[98] The CV of symmetric cells displayed four distinct peaks for the CNF/Mo/CNF electrode, however, there are no peaks observed for the CNF/CNF and CNF electrodes, revealing outstanding electrocatalytic activity of Mo nanoclusters in propelling LiPSs conversion. When using a high sulfur mass loading of 7.64 mg cm^{-2}, the specific capacity could reach up to 782.7 mAh g^{-1} at the initial cycle and maintained at 621.4 mAh g^{-1} after 100 cycles at 2C, which is comparable to commercial Li-ion batteries. Besides, Li et al. induced the Mo clusters in the N-doped carbon shells, and used them as the electrode-separator membranes for Li–S batteries.[99] The DFT calculation revealed the job-synergistic catalytic mechanism of the Mo clusters and N atoms to promote the deposition and decomposition of Li_2S during the electrochemical process. As shown in Figure 12d, the Li_2S dissociation barrier energies are 1.58, 1.05, and 0.19 eV for NC, Mo_{13}@NC-a (Mo clusters dispersed on the NC), and Mo_{13}@NC-b (some clusters occupy the N sites and the defection), respectively, revealing that the Li_2S dissociation on Mo_{13}@NC-b surface is more thermodynamically favorable. And the diffusion barrier energies are 0.21, 0.14, and 0.40 eV for NC, Mo_{13}@NC-a, and Mo_{13}@NC-b, these results also proved that the Li^+ release from the Mo clusters is facilitated during the Li_2S dissociation process.

Overall, various Mo-based catalytic materials are employed for Li–S batteries and exhibit certain electrochemical activity. Although several above-mentioned Mo-based catalysts show potential for Li–S batteries, more efforts should be devoted to

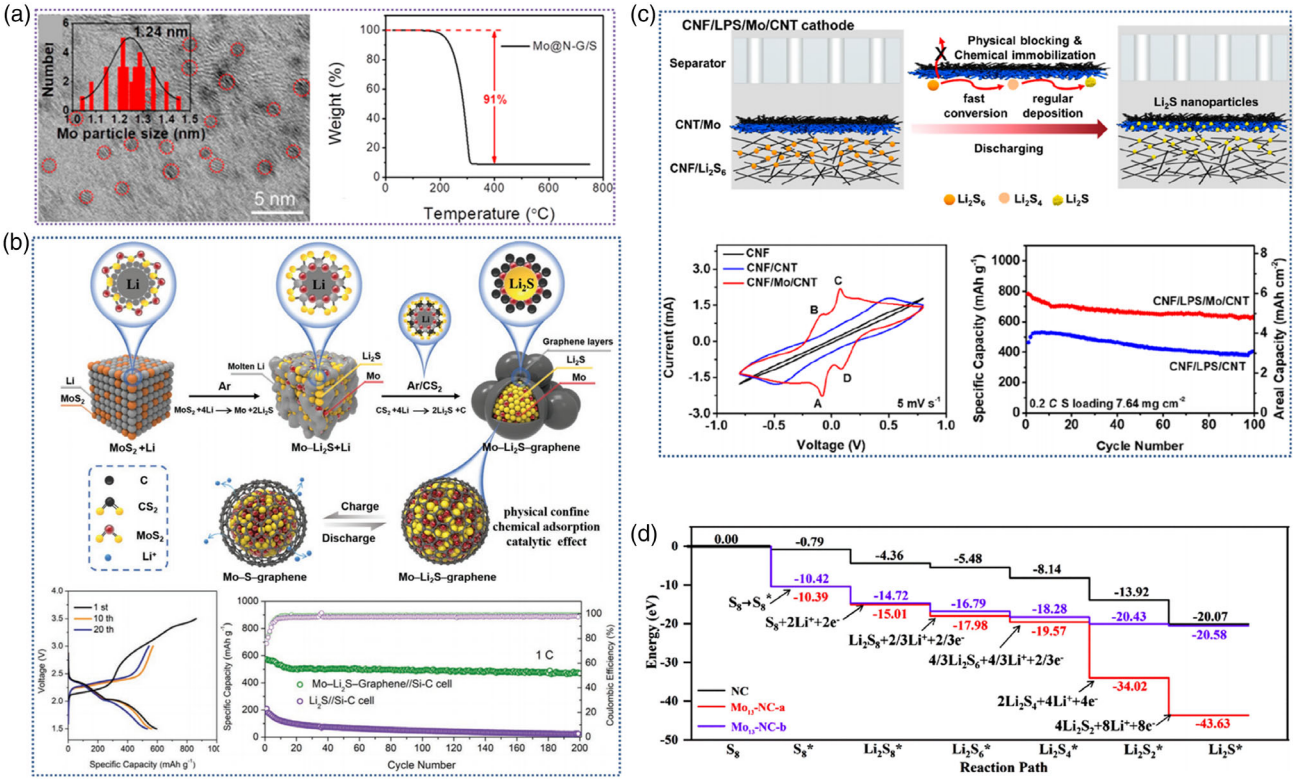

Figure 12. Mo-based metal/single atoms/cluster used for Li–S batteries. a) HRTEM of the Mo particle, and TGA curve of the Mo@N–G/S cathode. Reproduced with permission.[95] Copyright 2021, American Chemical Society. b) Schematic illustration showing the material synthesis and proposed electrochemical reaction mechanism of the Mo–Li_2S–graphene nanocapsules, voltage profiles of Mo–Li_2S–graphene//Si–C cell at 1.0C rate, and cycle performance. Reproduced with permission.[96] Copyright 2021, Wiley-VCH. c) Schematic illustration of the electrochemical behavior of the CNF/LPS/Mo/CNT cathodes, CV curve of symmetric cells, and cycling performance of the CNF/LPS/Mo/CNT cathode with high sulfur mass loading of 7.64 mg cm^{-2} at 0.2C. Reproduced with permission.[98] Copyright 2019, American Chemical Society. d) Energy change profiles of the total charge process on different surfaces. Reproduced with permission.[99] Copyright 2021, Elsevier.

the efficient, low-cost, controllable, and scalable synthesis, and the underlying electrochemical mechanism of Mo-based catalytic materials.

4. Summary and Outlooks

This review focuses on the recent researches on Mo-based catalytic materials for Li–S batteries. The Mo-based materials are ideal candidates for the hosts, separators, and interlayers for Li–S batteries, mainly because the Mo-based mediators can anchor the LiPSs and accelerate their conversion. Thus, the specific capacity, rate capability, and long-term cycling performance of Li–S batteries have been improved significantly (**Table 1**). Despite the encouraging progress, there is still a long way to go for the Mo-based catalytic materials before the practical applications of Li–S batteries. Therefore, further efforts may be focused on the following aspects.

4.1. Precise Synthesis of Catalytic Materials

To chemically prevent the shuttle effect, ideal catalytic materials should integrate the chemical/physical confinement and electrocatalytic interactions. The catalytic materials with high surface area, dense active sites, tunable doping, and controlled phase selectivity also need to be considered. Thus, the development of Mo-based catalytic materials with controllable synthesis under moderate conditions is necessary. Furthermore, the synthesis method should be sustainable, low-cost, and environment-friendly for practical applications.

4.2. Fundamental Understanding

The deposition of insulating Li_2S_2/Li_2S on the cathode active surface would increase the overpotential and internal resistance of the Li–S batteries, resulting in the fast decay of the reversible capacity. To date, most works focused on the liquid–solid conversion between LiPSs and Li_2S_2/Li_2S, neglecting the solid–solid conversion between Li_2S_2 and Li_2S. The latter process, however, will contribute about 50% of the capacity for Li–S batteries in theory. In this regard, Mo-based catalytic materials for the conversion between LiPSs and Li_2S_2/Li_2S, and between Li_2S_2 and Li_2S are urgently needed. Furthermore, in situ/ex situ electrochemical characterization and theoretical calculation of redox kinetics should be well investigated, such as X-ray diffraction, XPS, Raman spectroscopy, and microscopy techniques.

Table 1. Summary of the literature on various Mo-based catalytic materials for Li–S batteries.

Classification	Material	Preparation method (design strategies)	Particle size/ thickness	Sulfur content [wt%], areal sulfur loading [mg cm^{-2}], areal loading on the separator [mg cm^{-2}]	Electrolyte dosage [μL mg^{-1}]	Retained capacity [mAh g^{-1}], capacity retention [%], cycle number, and rate [C]	Reference
Cathode	WS_2 and MoS_2 flake	Chemical vapor deposition	100 nm (thickness)	N/A, N/A, N/A	N/A	596 mAh g^{-1}, 91%, 360, 0.5C	[10a]
Cathode	Graphene/MoS_2	Spray-drying approach	N/A	80 wt%, 2.1 mg cm^{-2}, N/A	N/A	1219 mAh g^{-1}, N/A, 200, 0.2C	[35b]
Cathode	MoS_2/S/rGO	Hydrothermal method and heat-treated	N/A	70 wt%, 1.0 mg cm^{-1}, N/A	N/A	954 mAh g^{-1}, 73.1%, 150, 0.2C	[36]
Cathode	MHCS@MoS_2–S	Solvothermal and annealing	300 nm (particle size)	72.1 wt%, 1.5 mg cm^{-1}, N/A	20 μL mg^{-1}	735.7 mAh g^{-1}, 75%, 500, 1C	[37]
Cathode	C@MoS_2	Solvothermal reaction	200 nm (particle size)	80 wt%, 6 mg cm^{-2}, 4 mg cm^{-2}	15 μL mg^{-1}	500 mAh g^{-1}, 70%, 1000, 2C	[38]
Separator	MoS_2@ graphene	One-pot solvothermal reaction	37.5 um (thickness)	87 wt%, 5.1 mg cm^{-2}, 5.3 mg cm^{-2}	6 μL mg^{-1}	752 mAh g^{-1}, 71%, 500, 1C	[39]
Separator	MoS_2@CNTP	Magnetron sputtering	N/A	70 wt%, 3.4 mg cm^{-2}, 0.0785 mg cm^{-2}	20 μL mg^{-1}	850 mAh g^{-1}, 50.7%, 100, 0.5C	[40b]
Separator	MoS_2	Slurry coating	20 um (thickness)	N/A, N/A, N/A	N/A	796 mAh g^{-1}, 93%, 500, 1C	[40c]
Separator	MoS_2/Celgard	Simple filtration	350 nm (particle size)	65 wt%, N/A, N/A	N/A	401 mAh g^{-1}, 50.2%, 600, 0.5C	[41]
Separator	PVDF//C–MoS_2	Slide coating method	20 um (thickness)	N/A, 3 mg cm^{-1}, N/A	N/A	434.4 mAh g^{-1}, 40%, 1500, 1 C	[43]
Separator	MoS_2/carbon nanotube	Chemical vapor deposition	N/A	50 wt%, 1.4 mg cm^{-2}, 0.25 mg cm^{-2}	25 μL mg^{-1}	770 mAh g^{-1}, 87.8%, 200, 0.5C	[44]
Cathode	MoS_2@NC	One-pot solvothermal process	200 nm (particle size)	60 wt%, 0.6 mg cm^{-2}, N/A	15 μL mg^{-1}	880 mAh g^{-1}, 80%, 100, 0.5C	[45]
Cathode	Layer-spacing-enlarged MoS_2	solvothermal reaction	N/A	N/A, 2.2 mg cm^{-2}, N/A	5.7 μL mg^{-1}	887 mAh g^{-1}, 70%, 500, 1C	[46]
Cathode	DCC@MoS_2/PrNP/ CNTs	Hydrothermal method followed by annealing	1–5 um (particle size)	72 wt%, 2.3 mg cm^{-2}, N/A	N/A	871 mAh g^{-1}, 84%, 800, 1C	[48]
Cathode	Co_9S_8@MoS_2/CNF	Electrospinning process	30–150 nm (particle size)	70 wt%, 3 mg cm^{-2}, N/A	17.69 μL mg^{-1}	794 mAh g^{-1}, 63.6%, 400, 1C	[49]
Cathode	GA-DR-MoS_2	One-step hydrothermal method	200–300 nm (particle size)	70 wt%, 1.5 mg cm^{-2}, N/A	N/A	821 mAh g^{-1}, 57.4%, 500, 0.2C	[53]
Cathode	MoS_2/NC	Pyrolysis of urea and thiourea served as a reductant	N/A	N/A, 0.21 mg cm^{-2}, N/A	N/A	1021 mAh g^{-1}, 81%, 100, 0.2C	[54]
Cathode	Co–MoS_2	Hydrothermal method	N/A	70 wt%, 5.27 mg cm^{-2}, N/A	30 μL mg^{-1}	705.1 mAh g^{-1}, 88.8%, 300, 0.2C	[55]
Cathode	P–MoS_2	Freeze-drying and annealing treatment	50–500 nm (particle size)	80 wt%, 1 mg cm^{-2}, N/A	15 μL mg^{-1}	629.4 mAh g^{-1}, 56.9%, 300, 0.5C	[56]
Cathode	CNT@MoS_2–B	Hydrothermal reaction and annealing treatment	N/A	N/A, 1.5 mg cm^{-2}, N/A	N/A	1035 mAh g^{-1}, 84.2%, 100, 0.2C	[57]
Separator	$MoSe_2$/CNT	Hydrothermal method and annealing	N/A	75 wt%, 1.4 mg cm^{-2}, N/A	15 μL mg^{-1}	1235 mAh g^{-1}, N/A, 50, 0.1C	[58]
Cathode	$MoSe_2$@FC@Mo_2C	Spinning coating and hydrothermal	10–20 nm (particle size)	72.12 wt%, 5.5 mg cm^{-2}, N/A	5 μL mg^{-1}	688 mAh g^{-1}, 71%, 1000, 2C	[59]
Cathode	Co–$MoSe_2$/MXene	Hydrothermal and vacuum insulation	N/A	75 wt%, 1.5 mg cm^{-2}, N/A	12 μL mg^{-1}	670 mAh g^{-1}, 52.5%, 500, 0.5C	[61]

Table 1. Continued.

Classification	Material	Preparation method (design strategies)	Particle size/ thickness	Sulfur content [wt%], areal sulfur loading [mg cm^{-2}], areal loading on the separator [mg cm^{-2}]	Electrolyte dosage [μL mg^{-1}]	Retained capacity [mAh g^{-1}], capacity retention [%], cycle number, and rate [C]	Reference
Separator	MoC@Ni−NCNT	CVD method	10 um (thickness)	N/A, 2 mg cm^{-2}, N/A	N/A	1007 mAh g^{-1}, 81.3%, 300, 0.5C	[67]
Cathode	Mo_2C–C nano-octahedrons	MOFs assisted strategy	800 nm (particle)	72.15 wt%, 2.1 mg cm^{-2}, N/A	N/A	600 mAh g^{-1}, 40%, 600, 1C	[70]
Cathode	Graphene@Mo_2C	Freeze drying and annealing process	3 nm (particle size)	70 wt%, 3.5 mg cm^{-1}, N/A	10 μL mg^{-1}	597 mAh g^{-1}, 69.4%, 600,1C	[74]
Cathode	Mesoporous, conductive Mo_2N	Silica template and HF etching	N/A	N/A, 1.1 mg cm^{-2}, N/A	N/A	914 mAh g^{-1}, 91.8%, 100, 0.5C	[76]
Separator	MoN@CNFs	Preoxidation stabilization and annealing treatment	8.4 um (thickness)	70 wt%, 1 mg cm^{-2}, 0.37 mg cm^{-2}	15 μL mg^{-1}	645 mAh g^{-1}, 75.1%, 300, 1C	[78]
Cathode	MoS_2–MoN	Hydrothermal process	N/A	N/A, 1.2 mg cm^{-2}, N/A	6.3 μL mg^{-1}	520 mAh g^{-1}, 61%, 1000, 1C	[81]
Separator	rGO/MoO_2	Hydrothermal method	2 um (thickness)	80 wt%, 2.1 mg cm^{-2}, 0.166 mg cm^{-2}	20 μL mg^{-1}	757.5 mAh g^{-1}, 58.6%, 200, 0.2C	[84]
Cathode	MoO_3–CP	Hydrothermal method and annealing	100–2000 nm (particle size)	N/A, 3 mg cm^{-2}, N/A	N/A	976 mAh g^{-1}, 85.2%, 1000, 1C	[87]
Cathode	MoO_2/MoS_2@CC	Chemical vapor deposition	3.4 um (thickness)	N/A, 4 mg cm^{-2}, N/A	15 μL mg^{-1}	640 mAh g^{-1}, 70%, 140, 1C	[88]
Cathode	MoO_2/α-MoC	Acid etching and carbonization	N/A	80 wt%, 1.2 mg cm^{-2}, N/A	15 μL mg^{-1}	735 mAh g^{-1}, 74.3%, 300, 0.5C	[89]
Cathode	HCS–Ru–Mo_4P_3	NaoH etching and annealing	5 nm (particle size)	77 wt%, 2 mg cm^{-2}, N/A	N/A	582.5 mAh g^{-1}, 61%, 350, 1C	[91]
Separator	MoP–MoS_2/PCNF	Hydrothermal method and annealing	500 nm (particle size)	70 wt%, 2.2 mg cm^{-2}, N/A	N/A	793.6 mAh g^{-1}, 75.5%, 400, 2C	[93]
Cathode	Mo@N–G	Freeze drying and annealing treatment	1.24 nm (particle size)	90 wt%, 1 mg cm^{-2}, N/A	N/A	1261 mAh g^{-1}, 92.7%, 100, 0.2C	[95]
Cathode/ Separator	CNF/LPS/Mo/CNT	Vacuum filtration method	5 um (thickness)	N/A, 1.91 mg cm^{-2}, 0.05 mg cm^{-2}	N/A	744 mAh g^{-1}, 70%, 500, 1C	[98]

4.3. Safety Issue

Solid-state electrolytes have attracted much attention due to their reliable safety and the ability to inhibit the shuttle effect, which may be one of the alternative strategies for high-safety Li–S batteries.[100] Solid-state electrolytes with Mo-based catalytic materials will accelerate the redox kinetics of sulfur and the electrolyte/electrode interface, thus achieving high-safety Li–S batteries with high-energy density.

4.4. Practical Application

Achieving the commercialization of Li–S batteries requires comprehensive evaluation under the conditions of high sulfur loading, large charge/discharge current rate, lean electrolyte, and low lithium consumption. In addition, the amount of catalytic material should be as low as possible, to maintain the overall energy density. Only under such strict conditions can Li–S batteries with Mo-based catalytic materials achieve superb energy density to exceed those of Li-ion batteries and other emerging energy storage systems.

In summary, significant progress has been achieved in the research in the research of Mo-based catalytic materials. However, the practical applications of high-energy-density Li–S batteries are still hindered by several challenges, thus requiring further efforts on synthesizing highly efficient catalytic materials and on developing a deeper understanding of the underlying mechanisms on a molecular/atom level. It is also expected that the rapid development of Mo-based catalytic materials in Li–S batteries will provide fundamental guidance for other related energy storage systems, such as Li–Se batteries, and Na–S batteries.

Acknowledgements

The authors gratefully acknowledge the financial support provided by the Chongqing Institute of Green and Intelligent Technology, Chinese Academy of Sciences (No. E2906216).

Conflict of Interest

The authors declare no conflict of interest.

Keywords

catalytic materials, Li–S batteries, molybdenum, shuttle effects, sluggish kinetics

Received: October 19, 2022
Revised: December 5, 2022
Published online: December 16, 2022

[1] J. B. Goodenough, K. S. Park, *J. Am. Chem. Soc.* **2013**, *135*, 1167.
[2] a) P. G. Bruce, S. A. Freunberger, L. J. Hardwick, J. M. Tarascon, *Nat. Mater.* **2012**, *11*, 19; b) Y. Yang, G. Y. Zheng, Y. Cui, *Chem. Soc. Rev.* **2013**, *42*, 3018; c) A. Manthiram, Y. Z. Fu, S. H. Chung, C. X. Zu, Y. S. Su, *Chem. Rev.* **2014**, *114*, 11751; d) D. Larcher, J. M. Tarascon, *Nat. Chem.* **2015**, *7*, 19; e) Q. Pang, X. Liang, C. Y. Kwok, L. F. Nazar, *Nat. Energy* **2016**, *1*, 1.
[3] a) X. L. Ji, K. T. Lee, L. F. Nazar, *Nat. Mater.* **2009**, *8*, 500; b) Z. Li, J. T. Zhang, X. W. Lou, *Angew. Chem. Int. Ed.* **2015**, *54*, 12886; c) H. Yuan, J. Q. Huang, H. J. Peng, M. M. Titirici, R. Xiang, R. J. Chen, Q. B. Liu, Q. Zhang, *Adv. Energy Mater.* **2018**, *8*, 1802107; d) J. P. Yue, M. Yan, Y. X. Yin, Y. G. Guo, *Adv. Funct. Mater.* **2018**, *28*, 1707533; e) J. R. He, A. Manthiram, *Energy Storage Mater.* **2019**, *20*, 55; f) F. Li, J. Liu, J. He, Y. Hou, H. Wang, D. Wu, J. Huang, J. Ma, *Angew. Chem. Int. Ed.* **2022**, *61*, 202205091; g) H. Wang, J. Liu, J. He, S. Qi, M. Wu, F. Li, J. Huang, Y. Huang, J. Ma, *eScience* **2022**, *2*, 557.
[4] a) L. W. Ji, M. M. Rao, S. Aloni, L. Wang, E. J. Cairns, Y. G. Zhang, *Energy Environ. Sci.* **2011**, *4*, 5053; b) S. Xin, L. Gu, N. H. Zhao, Y. X. Yin, L. J. Zhou, Y. G. Guo, L. J. Wan, *J. Am. Chem. Soc.* **2012**, *134*, 18510.
[5] a) L. Kong, X. Chen, B. Q. Li, H. J. Peng, J. Q. Huang, J. Xie, Q. Zhang, *Adv. Mater.* **2018**, *30*, 1705219; b) Z. Li, H. B. Wu, X. W. Lou, *Energy Environ. Sci.* **2016**, *9*, 3061; c) X. Y. Tao, J. G. Wang, C. Liu, H. T. Wang, H. B. Yao, G. Y. Zheng, Z. W. Seh, Q. X. Cai, W. Y. Li, G. M. Zhou, C. X. Zu, Y. Cui, *Nat. Commun.* **2016**, *7*, 1; d) J. R. He, Y. F. Chen, A. Manthiram, *Energy Environ. Sci.* **2018**, *11*, 2560; e) Q. Wang, H. Zhao, B. Li, C. Yang, M. Li, Y. Li, P. Han, M. Wu, T. Li, R. Liu, *Chinese Chem. Lett.* **2021**, *32*, 1157.
[6] J. Park, S. H. Yu, Y. E. Sung, *Nano Today* **2018**, *18*, 35.
[7] S. Sun, B. Liu, H. S. Zhang, Q. B. Guo, Q. Y. Xia, T. Zhai, H. Xia, *Adv. Energy Mater.* **2021**, *11*, 2003599.
[8] a) Y. Liu, S. Ma, L. Liu, J. Koch, M. Rosebrock, T. Li, F. Bettels, T. He, H. Pfnür, N. C. Bigall, F. Ding, L. Zhang, *Adv. Funct. Mater.* **2020**, *30*, 2002462; b) D. H. Liu, C. Zhang, G. M. Zhou, W. Lv, G. W. Ling, L. J. Zhi, Q. H. Yang, *Adv. Sci.* **2018**, *5*, 1700270; c) J. Lei, T. Liu, J. J. Chen, M. S. Zheng, Q. Zhang, B. W. Mao, Q. F. Dong, *Chem* **2020**, *6*, 2533.
[9] a) S. Imtiaz, Z. A. Zafar, R. Razaq, D. Sun, Y. Xin, Q. Li, Z. L. Zhang, L. Zheng, Y. H. Huang, J. A. Anderson, *Adv. Mater. Interfaces* **2018**, *5*, 1800243; b) C. Lin, L. B. Qu, J. T. Li, Z. Y. Cai, H. Y. Liu, P. He, X. Xu, L. Q. Mai, *Nano Res.* **2019**, *12*, 205.
[10] a) G. Babu, N. Masurkar, H. Al Salem, L. M. R. Arave, *J. Am. Chem. Soc.* **2017**, *139*, 171; b) J. Park, B. C. Yu, J. S. Park, J. W. Choi, C. Kim, Y. E. Sung, J. B. Goodenough, *Adv. Energy Mater.* **2017**, *7*, 1602567.
[11] G. S. Jiang, F. Xu, S. H. Yang, J. P. Wu, B. Q. Wei, H. Q. Wang, *J. Power. Sources* **2018**, *395*, 77.
[12] a) Y. L. Wu, X. R. Zhu, P. R. Li, T. Zhang, M. Li, J. Deng, Y. Huang, P. Ding, S. X. Wang, R. Zhang, J. Lu, G. Lu, Y. F. Li, Y. G. Li, *Nano Energy* **2019**, *59*, 636; b) Y. Y. Li, S. S. Yao, C. J. Zhang, Y. P. He, Y. Q. Wang, Y. Z. Liang, X. Q. Shen, T. B. Li, S. B. Qin, W. Wen, *Int. J. Energy Res.* **2020**, *44*, 8388.
[13] M. L. Wang, Y. Z. Song, Z. T. Sun, Y. L. Shao, C. H. Wei, Z. Xia, Z. N. Tian, Z. F. Liu, J. Y. Sun, *ACS Nano* **2019**, *13*, 13235.
[14] a) Z. Z. Du, X. J. Chen, W. Hu, C. H. Chuang, S. Xie, A. J. Hu, W. S. Yan, X. H. Kong, X. J. Wu, H. X. Ji, L. J. Wan, *J. Am. Chem. Soc.* **2019**, *141*, 3977; b) L. L. Zhang, D. B. Liu, Z. Muhammad, F. Wan, W. Xie, Y. J. Wang, L. Song, Z. Q. Niu, J. Chen, *Adv. Mater.* **2019**, *31*, 1903955; c) F. F. Wang, J. Li, J. Zhao, Y. X. Yang, C. L. Su, Y. L. Zhong, Q. H. Yang, J. Lu, *ACS Mater. Lett.* **2020**, *2*, 1450.
[15] a) W. G. Lim, S. Kim, C. Jo, J. Lee, *Angew. Chem. Int. Ed.* **2019**, *58*, 18746; b) S. J. Kim, K. Kim, J. Park, Y. E. Sung, *Chemcatchem* **2019**, *11*, 2373; c) H. J. Zhou, C. L. Song, L. P. Si, X. J. Hong, Y. P. Cai, *Catalysts* **2020**, *10*, 682; d) M. Zhang, W. Chen, L. X. Xue, Y. Jiao, T. Y. Lei, J. W. Chu, J. W. Huang, C. H. Gong, C. Y. Yan, Y. C. Yan, Y. Hu, X. F. Wang, J. Xiong, *Adv. Energy Mater.* **2020**, *10*, 2000082; e) P. Wang, B. J. Xi, M. Huang, W. H. Chen, J. K. Feng, S. L. Xiong, *Adv. Energy Mater.* **2021**, *11*, 2002893.
[16] H. Danuta, U. Juliusz, D. Herbert, J. Ulam, US3043896A, **1962**.
[17] a) K. Kumaresan, Y. Mikhaylik, R. E. White, *J. Electrochem. Soc.* **2008**, *155*, 576; b) H. Yamin, E. Peled, *J. Power Sources* **1983**, *9*, 281; c) R. Fang, S. Zhao, Z. Sun, D. W. Wang, H. M. Cheng, F. Li, *Adv. Mater.* **2017**, *29*, 1606823.
[18] W. Yang, W. Yang, L. Dong, X. Gao, G. Wang, G. Shao, *J. Mater. Chem. A* **2019**, *7*, 13103.
[19] S. Walus, C. Barchasz, R. Bouchet, J. F. Martin, J. C. Lepretre, F. Alloin, *Electrochim. Acta.* **2015**, *180*, 178.
[20] a) T. Y. Lei, W. Chen, W. Q. Lv, J. W. Huang, J. Zhu, J. W. Chu, C. Y. Yan, C. Y. Wu, Y. C. Yan, W. D. He, J. Xiong, Y. R. Li, C. L. Yan, J. B. Goodenough, X. F. Duan, *Joule* **2018**, *2*, 2091; b) H. Q. Wang, W. C. Zhang, J. Z. Xu, Z. P. Guo, *Adv. Funct. Mater.* **2018**, *28*, 1707520.
[21] a) Y. Z. Song, W. L. Cai, L. Kong, J. S. Cai, Q. Zhang, J. Y. Sun, *Adv. Energy Mater.* **2020**, *10*, 1901075; b) T. Zhang, L. Zhang, L. Zhao, X. Huang, Y. Hou, *EnergyChem* **2020**, *2*, 100036.
[22] a) J.-J. Chen, R.-M. Yuan, J.-M. Feng, Q. Zhang, J.-X. Huang, G. Fu, M.-S. Zheng, B. Ren, Q.-F. Dong, *Chem. Mater.* **2015**, *27*, 2048; b) D. Guo, H. Wei, X. Chen, M. Liu, F. Ding, Z. Yang, Y. Yang, S. Wang, K. Yang, S. Huang, *J. Mater. Chem. A* **2017**, *5*, 18193.
[23] M. Wang, Q. Liang, J. Han, Y. Tao, D. Liu, C. Zhang, W. Lv, Q.-H. Yang, *Nano Res.* **2018**, *11*, 3480.
[24] a) J. Sun, Y. Sun, M. Pasta, G. Zhou, Y. Li, W. Liu, F. Xiong, Y. Cui, *Adv. Mater.* **2016**, *28*, 9797; b) L. Li, L. Chen, S. Mukherjee, J. Gao, H. Sun, Z. Liu, X. Ma, T. Gupta, C. V. Singh, W. Ren, *Adv. Mater.* **2017**, *29*, 1602734; c) Z.-L. Xu, S. Lin, N. Onofrio, L. Zhou, F. Shi, W. Lu, K. Kang, Q. Zhang, S. P. Lau, *Nat. Commun.* **2018**, *9*, 1.
[25] G. Babu, K. Ababtain, K. Ng, L. M. R. Arava, *Sci. Rep.* **2015**, *5*, 1.
[26] H. Ye, J. Sun, S. Zhang, H. Lin, T. Zhang, Q. Yao, J. Y. Lee, *ACS Nano* **2019**, *13*, 14208.
[27] G. Zhou, S. Zhao, T. Wang, S.-Z. Yang, B. Johannessen, H. Chen, C. Liu, Y. Ye, Y. Wu, Y. Peng, *Nano Lett.* **2019**, *20*, 1252.
[28] a) W. G. Lim, S. Kim, C. Jo, J. Lee, *Angew. Chem. Int. Ed.* **2019**, *131*, 18920; b) J. He, A. Manthiram, *Energy Storage Mater.* **2019**, *20*, 55.
[29] a) Y. Zhang, L. Tao, C. Xie, D. Wang, Y. Zou, R. Chen, Y. Wang, C. Jia, S. Wang, *Adv. Mater.* **2020**, *32*, 1905923; b) Y. Song, W. Zhao, L. Kong, L. Zhang, X. Zhu, Y. Shao, F. Ding, Q. Zhang, J. Sun, Z. Liu, *Energy Environ. Sci.* **2018**, *11*, 2620; c) C. Ye, Y. Jiao, H. Jin, A. D. Slattery, K. Davey, H. Wang, S. Z. Qiao, *Angew. Chem. Int. Ed.* **2018**, *57*, 16703; d) J. He, G. Hartmann, M. Lee, G. S. Hwang, Y. Chen, A. Manthiram, *Energy Environ. Sci.* **2019**, *12*, 344.

[30] F. Macdonald, D. R. Lide, *Abstr. Pap. Am. Chem. Soc.* **2003**, *225*, U552.
[31] a) R. Bjornsson, F. Neese, R. R. Schrock, O. Einsle, S. DeBeer, *J. Biol. Inorg. Chem.* **2015**, *20*, 447; b) C. Van Stappen, R. Davydov, Z. Y. Yang, R. Fan, Y. Guo, E. Bill, L. C. Seefeldt, B. M. Hoffman, S. DeBeer, *Inorg. Chem.* **2019**, *58*, 12365.
[32] Z. Zhuang, J. Huang, Y. Li, L. Zhou, L. Mai, *ChemElectroChem* **2019**, *6*, 3570.
[33] a) M. R. Gao, J. X. Liang, Y. R. Zheng, Y. F. Xu, J. Jiang, Q. Gao, J. Li, S. H. Yu, *Nat. Commun.* **2015**, *6*; b) M. R. Gao, M. K. Y. Chan, Y. G. Sun, *Nat. Commun.* **2015**, *6*; c) Z. C. Zhuan, J. Z. Huan, Y. Li, L. Zhou, L. Q. Mai, *Chemelectrochem* **2019**, *6*, 3570.
[34] G. Babu, N. Masurkar, H. Al Salem, L. M. R. Arava, *J. Am. Chem. Soc.* **2017**, *139*, 171.
[35] a) H. Dai, L. Wang, Y. Zhao, J. Xue, R. Zhou, C. Yu, J. An, J. Zhou, Q. Chen, G. Sun, W. Huang, *Research* **2021**, *2021*, 5130420; b) B. Yu, Y. Chen, Z. Wang, D. Chen, X. Wang, W. Zhang, J. He, W. He, *J. Power Sources* **2020**, *447*, 227364; c) H.-E. Wang, X. Li, N. Qin, X. Zhao, H. Cheng, G. Cao, W. Zhang, *J. Mater. Chem. A* **2019**, *7*, 12068.
[36] Y. Wei, Z. Kong, Y. Pan, Y. Cao, D. Long, J. Wang, W. Qiao, L. Ling, *J. Mater. Chem. A* **2018**, *6*, 5899.
[37] Q. Shao, P. Lu, L. Xu, D. Guo, J. Gao, Z.-S. Wu, J. Chen, *Energy Chem.* **2020**, *51*, 262.
[38] Q. Wu, Z. Yao, X. Zhou, J. Xu, F. Cao, C. Li, *ACS Nano* **2020**, *14*, 3365.
[39] Z. Cheng, Y. Chen, Y. Yang, L. Zhang, H. Pan, X. Fan, S. Xiang, Z. Zhang, *Adv. Energy Mater.* **2021**, *11*, 2003718.
[40] a) R. Wang, J. Li, Y. Zhang, P. Y. Li, J. D. Duan, M. Q. Tang, C. Yuan, *Ceram. Int.* **2020**, *46*, 19408; b) J. Li, Y. J. Jiang, F. R. Qin, J. Fang, K. Zhang, Y. Q. Lai, *J. Electroanal. Chem.* **2018**, *823*, 537; c) S. F. Liu, Z. F. Zhou, D. C. Liu, *Ceram. Int.* **2019**, *45*, 14415.
[41] Z. A. Ghazi, X. He, A. M. Khattak, N. A. Khan, B. Liang, A. Iqbal, J. Wang, H. Sin, L. Li, Z. Tang, *Adv. Mater.* **2017**, *29*, 1606817.
[42] J. Wu, H. Zeng, X. Li, X. Xiang, Y. Liao, Z. Xue, Y. Ye, X. Xie, *Adv. Energy Mater.* **2018**, *8*, 1802430.
[43] M. Waqas, A. Manzoor Soomro, S. Ali, S. Kumar, S. Chan, K. Hussain, F. Hussain Memon, S. Ahmed Shaikh, *ChemistrySelect* **2020**, *5*, 12009.
[44] L. Yan, N. Luo, W. Kong, S. Luo, H. Wu, K. Jiang, Q. Li, S. Fan, W. Duan, J. Wang, *J. Power Sources* **2018**, *389*, 169.
[45] J. Wu, X. Li, H. Zeng, Y. Xue, F. Chen, Z. Xue, Y. Ye, X. Xie, *J. Mater. Chem. A* **2019**, *7*, 7897.
[46] Y. Pan, L. Gong, X. Cheng, Y. Zhou, Y. Fu, J. Feng, H. Ahmed, H. Zhang, *ACS Nano* **2020**, *14*, 5917.
[47] G. Xu, R. Li, M. Li, Q. Zhang, B. Li, J. Guo, X. Wang, C. Yang, Y. Yu, *Chem. Eng. J.* **2022**, *434*, 134498.
[48] M. Chen, W. Xu, S. Jamil, S. Jiang, C. Huang, X. Wang, Y. Wang, H. Shu, K. Xiang, P. Zeng, *Small* **2018**, *14*, 1803134.
[49] B. Li, Q. Su, L. Yu, J. Zhang, G. Du, D. Wang, D. Han, M. Zhang, S. Ding, B. Xu, *ACS Nano* **2020**, *14*, 17285.
[50] D. Lei, W. Shang, X. Zhang, Y. Li, S. Qiao, Y. Zhong, X. Deng, X. Shi, Q. Zhang, C. Hao, *ACS Nano* **2021**, *15*, 20478.
[51] J. Zhang, G. Xu, Q. Zhang, X. Li, Y. Yang, L. Yang, J. Huang, G. Zhou, *Adv. Sci.* **2022**, *9*, 2201579.
[52] a) T. Xiong, Y. Zhang, W. S. V. Lee, J. Xue, *Adv. Energy Mater.* **2020**, *10*, 2001769; b) Z. Shi, M. Li, J. Sun, Z. Chen, *Adv. Energy Mater.* **2021**, *11*, 2100332; c) E. G. Seebauer, K. W. Noh, *Mater. Sci. Eng. R Rep.* **2010**, *70*, 151.
[53] M. Liu, C. Zhang, J. Su, X. Chen, T. Ma, T. Huang, A. Yu, *ACS Appl. Mater. Interfaces* **2019**, *11*, 20788.
[54] M. Zhen, S.-Q. Guo, B. Shen, *ACS Sustainable Chem. Eng.* **2020**, *8*, 13318.
[55] W. Liu, C. Luo, S. Zhang, B. Zhang, J. Ma, X. Wang, W. Liu, Z. Li, Q.-H. Yang, W. Lv, *ACS Nano* **2021**, *15*, 7491.
[56] F. Liu, N. Wang, C. Shi, J. Sha, L. Ma, E. Liu, N. Zhao, *Chem. Eng. J.* **2022**, *431*, 133923.
[57] D. Tian, X. Song, Y. Qiu, X. Sun, B. Jiang, C. Zhao, Y. Zhang, X. Xu, L. Fan, N. Zhang, *ACS Nano* **2021**, *15*, 16515.
[58] Z.-T. Shao, L.-L. Wu, Y. Yang, X.-Z. Ma, L. Li, H.-F. Ye, X.-T. Zhang, *New Carbon Mater.* **2021**, *36*, 219.
[59] Y. Xiao, Y. Liu, G. Qin, P. Han, X. Guo, S. Cao, F. Liu, *Compos. B. Eng.* **2020**, *193*, 108004.
[60] Q. Hao, G. Cui, Y. Zhang, J. Li, Z. Zhang, *Chem. Eng. J.* **2020**, *381*, 122672.
[61] W. Wang, L. Huai, S. Wu, J. Shan, J. Zhu, Z. Liu, L. Yue, Y. Li, *ACS Nano* **2021**, *15*, 11619.
[62] Z. Shi, Z. Sun, J. Cai, X. Yang, C. Wei, M. Wang, Y. Ding, J. Sun, *Adv. Mater.* **2021**, *33*, 2103050.
[63] B. Yu, A. Huang, K. Srinivas, X. Zhang, F. Ma, X. Wang, D. Chen, B. Wang, W. Zhang, Z. Wang, *ACS Nano* **2021**, *15*, 13279.
[64] Y. Liu, G. Yu, G. D. Li, Y. Sun, T. Asefa, W. Chen, X. Zou, *Angew. Chem. Int. Ed.* **2015**, *127*, 10902.
[65] Z. Wang, X. Xu, Z. Liu, S. Ji, S. O. A. Idris, J. Liu, *Electrochim. Acta.* **2020**, *332*, 135482.
[66] P. Wang, Y. Song, Z. Xu, N. Li, J. Sun, B. Hong, Y. Lai, *Inorg. Chem. Front.* **2022**, *9*, 2194.
[67] B. Qin, Y. Cai, X. Si, C. Li, J. Cao, W. Fei, H. Xie, J. Qi, *ACS Appl. Mater. Interfaces* **2021**, *13*, 39424.
[68] a) H. B. Wu, B. Y. Xia, L. Yu, X.-Y. Yu, X. W. D. Lou, *Nat. Commun.* **2015**, *6*, 1; b) Y. Huang, Q. Gong, X. Song, K. Feng, K. Nie, F. Zhao, Y. Wang, M. Zeng, J. Zhong, Y. Li, *ACS Nano* **2016**, *10*, 11337.
[69] B. Yu, D. Chen, Z. Wang, F. Qi, X. Zhang, X. Wang, Y. Hu, B. Wang, W. Zhang, Y. Chen, *Chem. Eng. J.* **2020**, *399*, 125837.
[70] G. Chen, Y. Li, W. Zhong, F. Zheng, J. Hu, X. Ji, W. Liu, C. Yang, Z. Lin, M. Liu, *Energy Storage Mater.* **2020**, *25*, 547.
[71] N. Jiang, G. Jiang, D. Niu, J. Mao, M. Chen, K. Li, Y. Li, *J. Energy Chem.* **2020**, *51*, 207.
[72] a) Y. L. Ding, P. Kopold, K. Hahn, P. A. Van Aken, J. Maier, Y. Yu, *Adv. Funct. Mater.* **2016**, *26*, 1112; b) F. Pei, L. Lin, D. Ou, Z. Zheng, S. Mo, X. Fang, N. Zheng, *Nat. Commun.* **2017**, *8*, 1.
[73] C. Shang, L. Cao, M. Yang, Z. Wang, M. Li, G. Zhou, X. Wang, Z. Lu, *Energy Storage Mater.* **2019**, *18*, 375.
[74] S. Niu, S.-W. Zhang, R. Shi, J. Wang, W. Wang, X. Chen, Z. Zhang, J. Miao, A. Amini, Y. Zhao, *Energy Storage Mater.* **2020**, *33*, 73.
[75] Y. Zhu, X. Wu, M. Li, Y. Ji, Q. Li, X. He, Z. Lei, Z. Liu, R. Jiang, J. Sun, *ACS Sustainable Chem. Eng.* **2022**, *10*, 776.
[76] G. Jiang, F. Xu, S. Yang, J. Wu, B. Wei, H. Wang, *J. Power Sources* **2018**, *395*, 77.
[77] H. Liu, Z. Chen, H. Man, S. Yang, Y. Song, F. Fang, R. Che, D. Sun, *J. Alloys Compd.* **2020**, *842*, 155764.
[78] T. Tan, N. Chen, Z. Wang, Z. Tang, H. Zhang, Q. Lai, Y. Liang, *ACS Appl. Energy Mater.* **2022**, *5*, 6654.
[79] a) H. Shi, W. Lv, C. Zhang, D. W. Wang, G. Ling, Y. He, F. Kang, Q. H. Yang, *Adv. Funct. Mater.* **2018**, *28*, 1800508; b) H. Yuan, H. J. Peng, J. Q. Huang, Q. Zhang, *Adv. Mater. Interfaces* **2019**, *6*, 1802046.
[80] J.-L. Yang, S.-X. Zhao, Y.-M. Lu, X.-T. Zeng, W. Lv, G.-Z. Cao, *Nano Energy* **2020**, *68*, 104356.
[81] S. Wang, S. Feng, J. Liang, Q. Su, F. Zhao, H. Song, M. Zheng, Q. Sun, Z. Song, X. Jia, *Adv. Energy Mater.* **2021**, *11*, 2003314.
[82] Y.-N. Zhou, J. Ma, E. Hu, X. Yu, L. Gu, K.-W. Nam, L. Chen, Z. Wang, X.-Q. Yang, *Nat. Commun.* **2014**, *5*, 1.
[83] a) J. Haber, E. Lalik, *Catal. Today* **1997**, *33*, 119; b) L. Li, T. Zhang, J. Yan, X. Cai, S. Liu, *Small* **2017**, *13*, 1700441.
[84] K. Xu, X. Liang, L.-L. Wang, Y. Wang, J.-F. Yun, Y. Sun, H.-F. Xiang, *Rare Met.* **2021**, *40*, 2810.

[85] Y. Li, J. Zhang, C. Zhou, M. Ling, J. Lu, Y. Hou, Q. Zhang, Q. He, X. Zhan, F. Chen, *J. Alloys Compd.* **2020**, *826*, 154197.
[86] P. Ji, B. Shang, Q. Peng, X. Hu, J. Wei, *J. Power Sources* **2018**, *400*, 572.
[87] R. Zhang, M. Wu, X. Fan, H. Jiang, T. Zhao, *J. Power Sources* **2019**, *436*, 226840.
[88] Y. Tang, Y. Huang, L. Luo, D. E. Fan, Y. Lu, A. Manthiram, *Electrochim. Acta.* **2021**, *367*, 137482.
[89] D.-Q. Cai, J.-L. Yang, T. Liu, S.-X. Zhao, G. Cao, *Nano Energy* **2021**, *89*, 106452.
[90] Y. Mi, W. Liu, X. Li, J. Zhuang, H. Zhou, H. Wang, *Nano Research* **2017**, *10*, 3698.
[91] F. Ma, X. Wang, J. Wang, Y. Tian, J. Liang, Y. Fan, L. Wang, T. Wang, R. Cao, S. Jiao, *Electrochim. Acta.* **2020**, *330*, 135310.
[92] B. Yu, F. Ma, D. Chen, K. Srinivas, X. Zhang, X. Wang, B. Wang, W. Zhang, Z. Wang, W. He, *J. Mater. Sci. Technol.* **2021**, *90*, 37.
[93] X. Wang, N. Deng, J. Ju, G. Wang, L. Wei, H. Gao, B. Cheng, W. Kang, *J. Membr. Sci.* **2022**, *642*, 120003.
[94] Y. Xiao, Y. Li, Z. Guo, C. Tang, B. Sa, N. Miao, J. Zhou, Z. Sun, *Appl. Surf. Sci.* **2021**, *566*, 150634.
[95] Y. Liu, A. Chatterjee, P. Rusch, C. Wu, P. Nan, M. Peng, F. Bettels, T. Li, C. Ma, C. Zhang, B. Ge, N. C. Bigall, H. Pfnür, F. Ding, L. Zhang, *ACS Nano* **2021**, *15*, 15047.
[96] J. Zhang, J. Wang, M. Qian, B. Zhao, R. Wang, X. Hao, X. Huang, R. Shao, Z. Xing, J. Xie, *Adv. Funct. Mater.* **2022**, *32*, 2108305.
[97] D. Y. Guo, X. Zhang, M. L. Liu, Z. S. Yu, X. A. Chen, B. Yang, Z. Zhou, S. Wang, *Adv. Funct. Mater.* **2022**, *32*, 202204458.
[98] Y. Li, C. Wang, W. Wang, A. Y. S. Eng, M. Wan, L. Fu, E. Mao, G. Li, J. Tang, Z. W. Seh, *ACS Nano* **2019**, *14*, 1148.
[99] H. Jiang, S. Gu, J. Guo, Y. Dai, W. Zheng, X. Jiang, X. Wu, W. Xiao, G. He, X. Li, *Energy Storage Mater.* **2022**, *45*, 370.
[100] a) S. Li, W. Zhang, J. Zheng, M. Lv, H. Song, L. Du, *Adv. Energy Mater.* **2021**, *11*, 2000779; b) J. Yue, M. Yan, Y. X. Yin, Y. G. Guo, *Adv. Funct. Mater.* **2018**, *28*, 1707533.

Yuping Liu received his Ph.D. in Material Science & Engineering from Soochow University in 2018, then worked as a postdoctoral fellow in the Institute of Solid State Physics at Leibniz University Hannover in Germany from 2018 to 2022. Now, he is an associate professor at the Chongqing Institute of Green and Intelligent Technology, Chinese Academy of Sciences. His main research interests focus on nanomaterials for electrochemical energy storage and conversion, including rechargeable batteries and electrochemical capacitors.

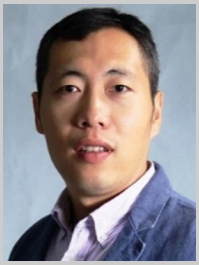

Shuangyi Liu received his Ph.D. in 2010 from The University of Hong Kong. After completing postdoctoral fellowship research, he moved to the Energy Institute of the City University of New York to continue his research career on nanomaterials for energy storage. He is currently a full professor and the Director of the Research Center for Electrochemical Energy Storage Technologies of Chongqing Institute of Green and Intelligent Technology, Chinese Academy of Sciences. He and his group are focusing on research and development of advanced electrochemical energy storage materials and devices.

Lin Zhang is currently a professor at Leibniz University Hannover, Germany. She received her B.S. and M.Sc. degrees from Beijing Normal University, China, then her Ph.D. degree (with honors) from Friedrich-Schiller University Jena, Germany. Her postdoctoral training was completed at Max Planck Institute for Solid State Physics (mentor: Prof. Martin Jansen) and IFW Dresden (mentor: Prof. Oliver G. Schmidt), respectively. In 2019, she was nominated for the famous Heinz-Maier Leibnitz prize. Her group is working on energy storage materials and devices, with a particular emphasis on material physics.